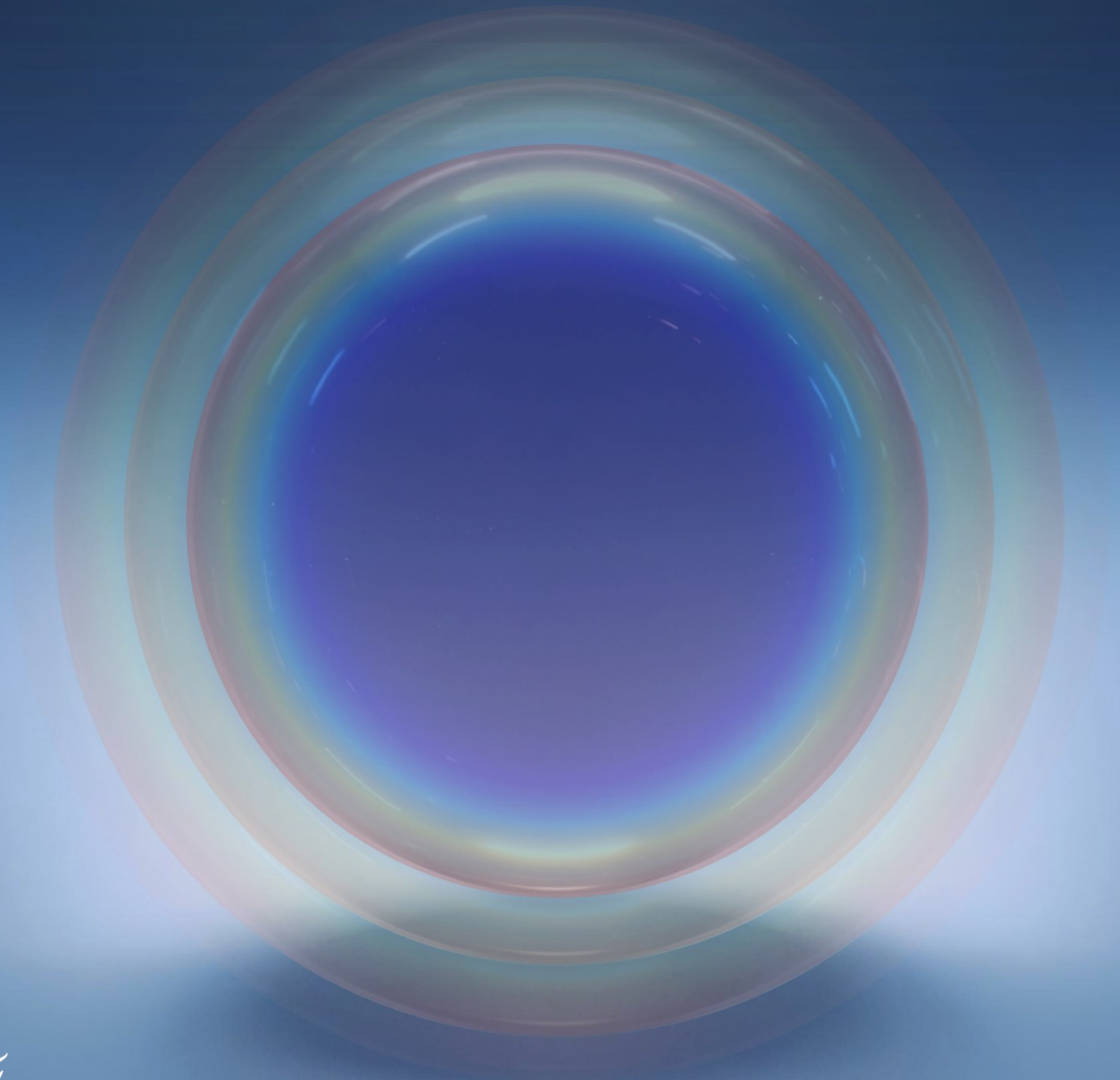MSc in Mechanical Engineering

Bubble dynamics in water electrolysis using multiphase Lattice Boltzmann Method

Michael Keith Parry Mujica

MSc Thesis Report

Bubble dynamics in water electrolysis using multiphase Lattice Boltzmann Method

Michael Keith Parry Mujica

27 September 2024

MSc Mechanical Engineering: Energy, Flow and Process Technology

The work in this thesis was carried out in the:

Complex Fluid Processing group
Delft University of Technology

Faculty supervisors:	Prof. dr. ir. Johan Padding
	Dr. ir. Remco Hartkamp
Daily supervisor:	Ir. Arvind Pari

Acknowledgements

Abstract

Hydrogen, as an energy carrier, is of paramount importance in the energy transition. At the industrial level, it can be derived from various sources, including fossil fuels, biomass, or electrolysis. In Alkaline Water Electrolysis (AWE), the growth of hydrogen bubbles directly impacts system efficiency. Understanding and simulating this growth, attributed to the diffusion of dissolved hydrogen in the supersaturated electrolyte near nucleation sites via diffusive and convective mass transfer, is a crucial step towards advancing knowledge in this field and unlocking new possibilities.

This research focuses on simulating the growth of a single hydrogen bubble in a supersaturated domain, both far from and near the cathode, in a 30 wt% KOH solution. Bubble growth, a mesoscale phenomenon, is investigated using the Lattice Boltzmann Method (LBM). A comprehensive comparison of the Shan-Chen (SC), Colour Gradient (RK), and Interface Tracking Phase-Field (HZC) methods was conducted to measure the intricacies of the multiphase system accurately. The Laplace Law equation served as a benchmark, demonstrating that the HZC method produced the most accurate results.

A continuous species transfer method is employed to track hydrogen transport from the supersaturated electrolyte into the bubble, validated with Newman's analytical solution of mass transfer controlled by pure diffusion inside a sphere. Two cases are then analyzed: one of a single bubble far from an electrode in a supersaturated domain and another of a single bubble near an electrode with a constant hydrogen flux. For the first case, bubble growth follows a power law equivalent to $R \sim t^{0.5}$, while in the second case, growth follows $R \sim t^{0.7}$, matching results from previous studies. Finally, this method is extended to a 3D model; however, the results cannot be directly compared to the 2D model due to the shorter runtime resulting from computational cost.

Contents

Contents

List of Figures

List of Tables

Nomenclature

<div align="center">Acronyms</div>

ADE	Advection Diffusion Equation
AWE	Alkaline Water Electrolysis
CFD	Computational Fluid Dynamics
FE	Free Energy
HER	Hydrogen Evolution Reaction
HZC	Interface Tracking Phase Field
LBE	Lattice Boltzmann Equation
LBM	Lattice Boltzmann Method
LBPM	Lattice Boltzmann Methods for Porous Media
MCMP	Multicomponent Multiphase
MRT	Multiple Relaxation Time
OER	Oxygen Evolution Reaction
PEM	Proton Exchange Membrane Electrolysis
PTV	Particle Tracking Velocimetry
RK	Colour-Gradient
SC	Shan-Chen
SCMP	Single Component Multiphase
SRT	Single Relaxation Time
SOEC	Solid Oxide Electrolyser Cell
TRT	Two Relaxation Time

<div align="center">Symbols</div>

$\boldsymbol{c_i}$	Discretised microscopic particle velocities
c_s	Lattice speed of sound
f	Distribution function
f^{eq}	Equilibrium distribution function
x	Particle position [m]
t	Time [s]
$\boldsymbol{u}$	Velocity [m/s]
w_i	Velocity set weights
Δt	Time step [s]
Δx	Spatial discretization [m]
$\boldsymbol{M}$	Transformation matrix
$\boldsymbol{S}$	Relaxation matrix
δ_E	Electrode boundary layer thickness [m]
δ_D	Bubble boundary layer thickness [m]
C_{H_2}	Concentration of hydrogen [mol/m^3]
D	Diffusivity coefficient [m^2/s]
He	Henry's Law

p	Pressure [bar]
ϕ	Phase field
ϕ_E	Equilibrium Potential [V]
R_c	Critical radius [m]
ν	Kinematic shear viscosity [m^2/s]
ρ	Macroscopic density [kg/m^3]
σ	Surface tension [N/m]
Ω	Collision operator

1. Introduction

The European Union's commitment to reducing carbon emissions, as outlined in the Paris Agreement, has prompted a significant shift towards cleaner energy sources. In 2022, the EU generated $2,641$ TWh of electricity, with a notable portion sourced from fossil fuels. However, as part of the EU's goal to achieve net-zero emissions by 2050, there's a growing emphasis on transitioning away from fossil fuels towards renewable energy sources [2].

Hydrogen, as one of the most promising clean and sustainable energy carriers, plays a pivotal role in this transition. Unlike traditional fossil fuels, hydrogen can be produced and consumed without carbon emissions. However, current methods of hydrogen production, primarily derived from fossil fuels like natural gas, pose challenges in terms of carbon emissions. Despite these challenges, hydrogen remains a crucial element in various industries, accounting for 2% of the total primary energy demand in 2018. Understanding the sources of hydrogen production, particularly from natural gas through processes like steam methane reforming, sheds light on the need for cleaner and more sustainable methods in line with the EU's emissions reduction goals.

Natural gas is the primary feedstock for approximately three-quarters of the annual global dedicated hydrogen production, totaling around 70 million tonnes of H_2. This reliance on approximately 205 billion cubic meters of natural gas annually accounts for 6% of global natural gas usage. Following closely behind is coal, contributing to an estimated 23% of global hydrogen production and consuming 107 Mt of coal annually, representing 2% of global coal use.

However, the significant dependence on natural gas and coal comes at an environmental cost. Presently, hydrogen production generates substantial carbon dioxide (CO_2) emissions, with emissions of approximately 10 tonnes of CO_2 per tonne of H_2 ($t\,CO_2/t\,H_2$) from natural gas, $12\ t\,CO_2/t\,H_2$ from oil products, and $19\ t\,CO_2/t\,H_2$ from coal. This results in approximately 830 Mt CO_2 annually. While various methods exist for hydrogen production, including steam reforming of natural gas, gasification of coal or biomass, and electrolysis, (see Fig. 1.1) it is essential to underscore the critical role hydrogen plays in the transition to a cleaner energy future [3]. Beyond its environmental benefits, hydrogen holds significant promise for addressing pressing energy challenges. Its versatility enables applications across diverse sectors, including transportation, industry, and energy storage. For instance, hydrogen fuel cells present a promising solution for decarbonizing transportation, offering zero-emission mobility with fast refuelling times and long driving ranges [3].

Moreover, hydrogen serves as a crucial enabler of renewable energy integration by facilitating the storage and conversion of excess renewable energy into storable forms. Through processes like electrolysis, surplus renewable electricity can be used to produce hydrogen, which can then be stored and later converted back into electricity or used as a feedstock for various industrial processes [3].

In addition to its role in decarbonizing energy systems, hydrogen holds strategic importance in enhancing energy security and fostering economic growth. As countries seek to
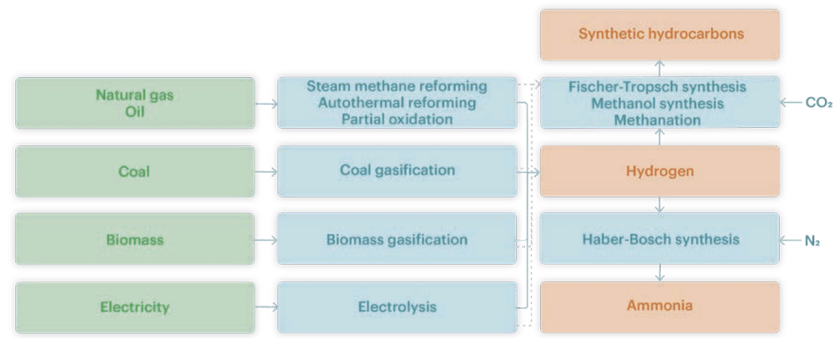
Figure 1.1.: Conventional H_2 production pathways [3].

diversify their energy sources and reduce reliance on fossil fuels, investments in hydrogen technologies can drive innovation, create jobs, and stimulate economic development [3].

Therefore, while discussing the various methods of hydrogen production provides valuable context, it is crucial to emphasize the broader significance of hydrogen as a clean, versatile, and strategically important energy carrier that can drive the transition to a sustainable energy future through electrochemical production.

1.1. Elecrochemical Hydrogen Production

The electrochemical hydrogen (H_2) production has been widely investigated for decades. At this stage, there are three industrially proven and used ways to produce H_2: Proton Exchange Membrane electrolysis (PEM), Solid Oxide Electrolyser Cell (SOEC), and Alkaline Water Electrolysis (AWE).

Proton membrane electrolysis uses a polymer membrane to separate the cell into an anode and cathode region, allowing protons to pass selectively. Water undergoes electrolysis at the anode, producing oxygen gas and hydrogen ions, which then move to the cathode through the membrane to form hydrogen gas. PEM electrolysis operates optimally at $40 - 60°C$, offering a promising avenue for hydrogen production with minimal carbon emissions. SOEC employ oxide-ion conducting ceramics as both the electrolyte and separator, operating at higher temperatures of $700 - 1000°C$. They offer high current densities and efficiencies, with ongoing research focusing on understanding and controlling degradation and thermomechanical stability. SOECs present a promising avenue for hydrogen production, particularly from renewable electricity, with the potential to operate as either fuel cells or electrolyser [4, 5]. The structure of the PEM electrolyser and the SOEC are shown in Figure 1.2.

1.1.1. Alkaline Water Electrolysis (AWE)

Alkaline water electrolysis holds a pivotal role in hydrogen production, rooted in its longstanding industrial application and enduring relevance in contemporary energy systems. At its core, AWE operates on the fundamental principle of water electrolysis under alkaline

(a) The working principle of a PEM electrolyser [4].

(b) The working principle of a SOEC [4].
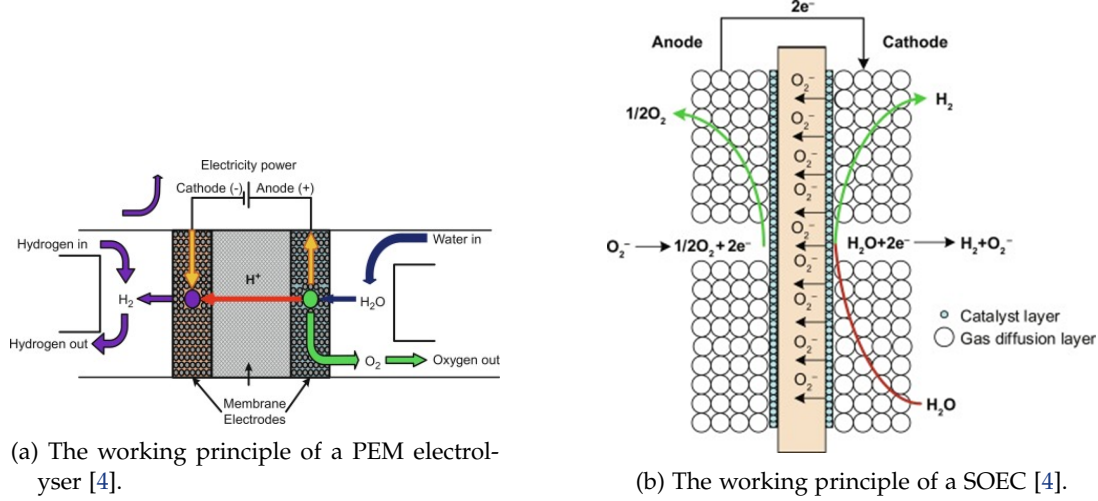
Figure 1.2.: Schematics for the PEM and SOEC devices.

conditions, leveraging an electrolyte, typically an alkaline aqueous solution like potassium hydroxide (KOH) at concentrations of $20 - 30$ wt%, to enhance ionic conductivity while mitigating electrode corrosion risks. The overall reactions of the system are shown (anode, cathode, total) as,

$$
\begin{aligned}
2\text{OH}^- &\rightarrow \frac{1}{2}\text{O}_2 + \text{H}_2\text{O} + 2\text{e}^-, \\
2\text{H}_2\text{O} + 2\text{e}^- &\rightarrow \text{H}_2 + 2\text{OH}^-, \\
2\text{H}_2\text{O} &\rightarrow \text{O}_2 + 2\text{H}_2.
\end{aligned}
\tag{1.1}
$$

The electrolytic process in AWE involves the reduction of water molecules at the cathode, yielding hydrogen gas, and the oxidation of hydroxyl ions at the anode, generating oxygen. These half-cell reactions, known as the hydrogen evolution reaction (HER) and the oxygen evolution reaction (OER) respectively, dictate the overall efficiency and performance of the electrolyser. The equilibrium potentials, ϕ_E of these reactions are governed by thermodynamic considerations, with the cathodic HER occurring at a potential of approximately -0.828 V and the anodic OER at approximately 0.4011 V under standard temperature and pressure [6]. Figure 1.3 shows the schematic of a AWE.

Nickel-based electrodes, typically porous to maximize interfacial surface area and reaction sites, are commonly employed in AWE systems. Operating within a voltage range of $1.4 - 3.0$ V, nominal current density range of $0.2 - 0.8$ A/cm^2, and electrode area range of $1 - 3$ m^2 industrial AWE can reach H$_2$ production rates of 1000 Nm^3/h [7, 8]. Production rates as the previously mentioned, coupled with the utilization of non-noble metal electrodes and the system's long-term stability, positions AWE as a commercially preferable solution over other electrolyser technologies. Nevertheless, AWE confronts challenges, notably its narrow operating power band and susceptibility to disruptions from fluctuations in power supply, particularly from renewable sources. The formation and evolution of hydrogen and oxygen bubbles during electrolysis further impede efficiency, necessitating ongoing research efforts to mitigate their impact and optimize AWE performance. Ultimately, advancements aimed at reducing costs and increasing efficiency are imperative to unlock the full potential of
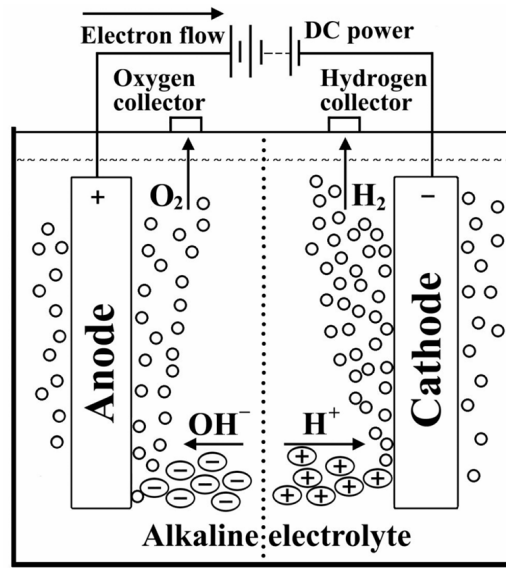
Figure 1.3.: The working principle of a AWE [9].

AWE and facilitate its widespread adoption in the transition towards sustainable hydrogen production [10].

1.2. Bubble dynamics in AWE

Hydrogen bubble growth in AWE occurs due to the diffusion of dissolved hydrogen in the surrounding supersaturated electrolyte in the cathode. Figure 1.4 shows a schematic of this process. The H_2 bubble will grow as the dissolved gas diffuses from the electrolyte, reducing the supersaturation of products in the electrolyte and distorting the equilibrium toward the products, ultimately reducing the concentration overpotential. This process occurs after the bubble nucleates and before the H_2 bubble detaches at a critical radius R_c, where the bubble growth is driven by mass transport caused by gradients in dissolved hydrogen concentration, especially near the electrodes and also by bubble coalescence. The critical radius at which the bubble detaches will vary, but generally, it is within $10 - 100$ μm [11].

Bubbles detach after the buoyant forces surpass the adhesion force due to surface tension between the bubble and the electrode. However, it is also believed that the Marangoni effect also plays a role in the bubble detachment process, as concentration gradients will increase bubble coalescing at the electrode-bubble interface for small overpotential regions [12]. After the bubble has detached, some hydrogen will still diffuse into the gaseous phase, although it is insignificant compared to the amount diffused into the gaseous phase before the bubbles detach. A better understanding of bubble dynamics is paramount, as the performance of electrolytic cells is heavily influenced by the formation of bubbles at higher current densities. Bubbles attached to the cathode surface reduce the active electrode area by decreasing the contact area between the electrode and electrolyte, thus increasing the Ohmic resistance and overpotential [13]. During their growth, hydrogen bubbles have minimal contact area with the electrode at low current densities since the bubbles shape will be more spherical, with
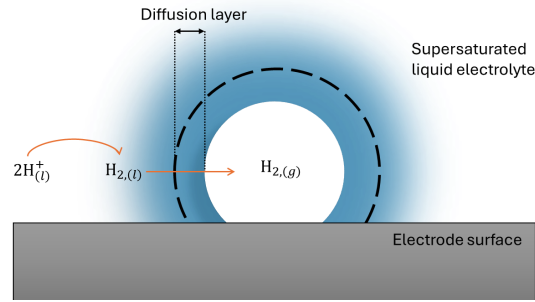
Figure 1.4.: Hydrogen diffusion from the liquid electrolyte phase info the gaseous phase in AWE schematic.

less spread on the electrode. As the current density increases -more hydrogen production per unit area- the contact angle further decreases due to the reduced surface tension at the metal-electrolyte interface. Additionally, the electric double layer may play an important role, as it is expected that this layer will be gradually displaced [14]. Bubble remanence time in the electrolyte also affects the electrical resistance. Nagai et al. [15] showed that the increase of volume fraction of H_2 bubbles between electrodes increases the electric resistance in the electrolyte, resulting in AWE inefficiency. The interaction between bubbles in the aqueous solution near the electrode or the bulk flow is also essential. Bubble coalescence was explored by Bashkatov et al. [16], and showed the contactless interaction that opposes buoyant forces are electric and hydrodynamic forces, which act over distances equal to 5 times the diameter of a nucleated bubble. These forces can paradoxically oppose the direction to which the buoyant forces act.

1.3. Computational methods for bubble dynamics in AWE

Experimentally, measuring individual bubble behaviour is a challenge. Particle tracking velocimetry (PTV) is effective for bubbles larger than 30 μm but fails to capture smaller bubbles [17]. The shortcomings of experimental techniques can be overcome using computational modelling, which will adequately capture the intricate details of bubble dynamics near the liquid and gas interface and also the mesoscale dynamics of the bubbles. The distinct features of H_2 bubble dynamics in AWE can occur on scales ranging from microns to millimetres, requiring a modelling method to capture these mesoscale phenomena adequately.

Conventional computational fluid dynamics (CFD) models focus on the macroscale. Other approaches, such as Molecular Dynamics, have been developed for the microscale; however, the computational cost is high. For mesoscale modelling, a relatively recent method has developed from the Boltzmann Equation called the Lattice Boltzmann Method (LBM). Several works of literature will be explored later, and the benefits of investigating bubble dynamics in AWE via LBM will be discussed. This suitability stems from LBM's capacity to effectively model multicomponent, multiphase physics. Different multiphase and multicomponent models have been copiously developed. However, the main ones are known as the Colour-Gradient model, the Shan-Chen model, the Free Energy model, and the Interface

Tracking model. Additionally, the rapid growth in the LBM has seen a surge of open-source code for porous media, making the use and implementation of new models available to a wide range of audiences. Codes such as Lattice Boltzmann Methods for Porous Media (LBPM) allow for further development and easy parallelization, a must for the computationally expensive models for bubble dynamics in AWE.

1.4. State of the art

The lattice Boltzmann method has emerged as a powerful tool for simulating complex multiphase flows, including immiscible fluid dynamics and interfacial phenomena [18–22]. Originating from cellular automata principles, the LBM provides a mesoscopic approach, bridging fluid dynamics' microscopic and macroscopic scales [18, 22]. This method has applications in various scenarios, such as bubble formation, droplet coalescence, rising bubbles, and flows in porous media [18–20].

As mentioned before, to model immiscible multiphase flows accurately, different LBM-based models have been developed, including the Rothman–Keller (RK); who developed the Colour-Gradient method, Shan–Chen (SC), Free Energy (FE) and interface tracking (HCZ) [18, 22]. Each model has advantages and limitations, offering varying levels of parameter flexibility, simplicity, and numerical stability, which will be discussed in Chapter 3.

Recent advancements in LBM modelling have focused on enhancing the accuracy and stability of simulations. For instance, the integration of recolouring algorithms, such as Latva-Kokko's recolouring operator, has shown promise in reducing spurious currents at interfaces, leading to improved simulation accuracy [18]. Additionally, models proposed by Lee et al. have demonstrated increased stability, enabling simulations of systems with high-density ratios, such as the gas-liquid systems of interest in the present study [22].

Experimental validation is crucial in refining LBM models and assessing their reliability. Numerical experiments closely aligned with established frameworks, such as those proposed by Reis and Phillips, provide valuable insights into the performance of LBM-based models across different scenarios.

Furthermore, the lattice Boltzmann approach has been extended to study interfacial convection phenomena, such as Rayleigh and Marangoni convection, which are essential in understanding mass and heat transfer processes across fluid interfaces. These studies shed light on the complex interplay between fluid properties, surface tension, and buoyancy forces, contributing to advancements in chemical engineering and related fields [21, 22].

The applications of multiphase models extend beyond academic research to practical domains such as inkjet printing, microfluidics, power engineering, and chemical engineering industries. These models are instrumental in optimising processes, understanding flow behaviour, and designing efficient devices for various applications, including bubble dispersion, drop formation, and interfacial mass transfer [20, 21].

More recent studies have investigated the invasion patterns of oxygen in water-saturated anodic porous transport layers in polymer electrolyte membrane water electrolyser, using a Shan-Chen multi-component LB model [23, 24]. Currently, the effects of H_2 bubbles at the cathode in AWE using multiphase lattice Boltzmann Methods is not well documented and is a clear area for development. The present work looks to address this gap.

1.5. Research objectives

The main objective of the present work will be to **implement a multiphase lattice Boltzmann method, allowing for species diffusion from the liquid phase of the electrolyte into the gaseous hydrogen phase, and track the consequent bubble growth.** Secondary objectives are set to ensure the completion of the main objective, which work as stepping stones. The secondary objectives are:

- Develop and implement a `"toy code"` in Python to simulate a static bubble using the Shan-Chen, Colour Gradient with enhanced equilibria and Phase-field interface tracking multiphase models. This step will serve as a comparative analysis to identify the most suitable and stable method for handling high-density ratios.

- Investigate the species balance at the bubble interface and propose an appropriate distribution function to accurately model the species flux.

- Explore bubble growth under a constant flux boundary condition in supersaturated and unsaturated domains.

- Validate the implementation of the multiphase model by comparing the results with those from Khalighi et al. and Brandon and Kelsall in a supersaturated stagnant fluid, ensuring the correctness and reliability of the LBM implementation.

- Extend the 2D model to a 3D model.

These objectives collectively aim to advance the understanding and simulation capabilities of the LBM simulations, particularly concerning multiphase transport phenomena in alkaline water electrolysis.

1.6. Report outline

The following chapter, Lattice Boltzmann Method, will briefly discuss the Lattice Boltzmann Method basics such as the different velocity sets, relaxation times and stability conditions for LBM simulations. Chapter three will then delve into three different multi-component and multiphase methods. A two-dimensional static bubble validation case is compared with Young–Laplace equation for a static bubble, substantiating the implementation of a the Phase-Field method for further bubble growth simulations. The methodology to capture the mass diffusion from the supersaturated electrolyte into the gaseous hydrogen phase is discussed in the fourth chapter. Implementing a multiple relaxation time (MRT) scheme is explored to enhance the stability of the concentration distribution function. As an approximation to a system which solves the Butler-Volmer kinetics at the electrode, a constant H_2 flux is implemented to compare with the supersaturated case, in chapter five. The sixth chapter consolidates the findings of the previous work in an endeavour to achieve the research objectives and proposes further work to improve the model.

2. Lattice Boltzmann Method

The lattice Boltzmann method (LBM) is a mesoscopic, particle-based approach that employs a simplified kinetic description rooted in classical statistical physics. In contrast to conventional numerical methods, which rely on discretizing macroscopic continuum equations, the LBM is founded on developing streamlined kinetic models to capture essential physics governing mesoscopic processes. This ensures that macroscopic averaged properties conform to specified macroscopic equations. The fundamental premise supporting the adoption of these simplified kinetic-type approaches in studying macroscopic fluid flows lies in the recognition that macroscopic fluid dynamics emerge from the collective behavior of numerous microscopic particles in the system. Furthermore, it asserts that macroscopic dynamics are minimally influenced by intricate details inherent in microscopic physics. Formulating simplified kinetic equations avoids the complexity of dealing with intricate equations like the full Boltzmann equation, thereby eliminating the need for molecular dynamics simulation that tracks each particle [27].

Electrochemical systems exhibit inherent multi-physics complexity, with their performance intricately governed by physical phenomena occurring at interfaces. Moreover, these systems involve the intricate coupling of various physics, encompassing processes such as the transport of ion/neutral species and electrochemical reactions. Therefore, to accurately predict the operation and performance of the system, the computational model must adeptly incorporate these diverse physics. The LBM's capacity to link mesoscopic quantities with macroscopic properties adds substantial value as a CFD tool, making it a preferred choice for developing this project.

2.1. Lattice Boltzmann Equation

The Lattice Boltzmann Equation (LBE) is represented by the continuous particle probability distribution function $f(\boldsymbol{x}, \boldsymbol{\xi}, t)$, which specifies the probability of encountering a particle at position $\boldsymbol{x}$ at time t with velocity $\boldsymbol{\xi}$. The evolution of these distributions due to interactions at the microscopic scale is described by [28]:

$$\frac{\partial f}{\partial t} + \boldsymbol{\xi} \cdot \frac{\partial f}{\partial \boldsymbol{x}} = \Omega(f). \tag{2.1}$$

The left-hand side, which resembles an advection-type expression, describes the force-free, free-streaming of particles, while the right-hand side contains the collision operator $\Omega(f)$. The collision operator describes the changes in the probability distribution function $f(\boldsymbol{x}, \boldsymbol{\xi}, t)$ induced by inter-particle collisions. While being very hard to solve analytically, the Boltzmann equation is relatively simple to solve numerically. The introduction of discretised microscopic particle velocities $\boldsymbol{c}_i = (c_{ix}, c_{iy}, c_{iz})$ offers a mean to discretize the porbability

distribution function f_i from its continuous version f. This leads to the discretized Boltzmann equations,

$$\frac{\partial f_i}{\partial t} + \boldsymbol{\xi}_i \cdot \frac{\partial f_i}{\partial \boldsymbol{x}_i} = \Omega_i(f_i). \tag{2.2}$$

The velocity space discretization will be dependent on the dimensions that are considered, but also the amount of velocity spaces. More information regarding the velocity space discretization is discussed in Section 2.3. By discretising Eq.2.2 in velocity space, physical space, and time, a fully discretised version of the lattice Boltzmann equation is obtained:

$$f_i(\boldsymbol{x} + \boldsymbol{c}_i \Delta t, t + \Delta t) - f_i(\boldsymbol{x}, t) = \Omega_i(\boldsymbol{x}, t), \tag{2.3}$$

where Δt represents the time step, which represents the time resolution in any set of units. The most common set of units used is lattice units, a simple artificial set of units such that $\Delta t = 1$. This is also generally applied with the spatial discretization, Δx. The discretised collision operator Ω_i has different methods of being approximated. The most simple approximation is given by the single relaxation time approximation developed by Bhatnagar, Gross and Krook (BGK) [29]:

$$\Omega_i = -\frac{\Delta t}{\tau} \left(f_i - f_i^{eq} \right), \tag{2.4}$$

where τ is known as the relaxation factor and f^{eq} as the local equilibrium distribution function, which is determined from the Maxwell distribution function, via Eq.2.5, where it is worth noting that the local equilibrium function depends on macroscopic quantities such as the density ρ, velocity $\boldsymbol{u}$ and temperature T.

$$f^{eq}(\rho, \boldsymbol{u}, T, \boldsymbol{\xi}) = \frac{\rho}{(2\pi RT)^{d/2}} exp(-\frac{(\boldsymbol{\xi} - \boldsymbol{u})^2}{2RT}). \tag{2.5}$$

To discretise the equilibrium distribution function, the series expansion of the Hermite Polynomial up to the third term is enough to recover the macroscopic laws for hydrodynamics. By doing so, the discrete form of the equilibrium distribution reads as,

$$f_i^{eq} = w_i \rho \left(1 + \frac{\boldsymbol{u} \cdot \boldsymbol{c}_i}{c_s^2} + \frac{(\boldsymbol{u} \cdot \boldsymbol{c}_i)^2}{2c_s^4} - \frac{\boldsymbol{u} \cdot \boldsymbol{u}}{2c_s^2} \right), \tag{2.6}$$

where $\boldsymbol{c}_i = \boldsymbol{\xi}_i / \sqrt{3}$ is a further simplification to introduce the particle velocity and w_i is its respective velocity set weights. The link between the LBE and the Navier-Stokes equations is established through the Chapman-Enskog analysis [30], which yields the kinematic shear viscosity dependent on the relaxation time, as shown by Eq. 2.7:

$$\nu = c_s^2 \left(\tau - \frac{\Delta t}{2} \right). \tag{2.7}$$

The macroscopic components of the flow, such as density and momentum (and hence velocity), are determined by the zeroth and first-order moments, as shown in Eqs. 2.8 - 2.9, respectively,

$$\rho(\boldsymbol{x}, t) = \sum_i f_i(\boldsymbol{x}, t), \tag{2.8}$$

$$\rho \boldsymbol{u}(\boldsymbol{x}, t) = \sum_i \boldsymbol{c}_i f_i(\boldsymbol{x}, t). \tag{2.9}$$

2.2. Forces in LBE

In most hydrodynamic problems, forcing terms are present and require proper evaluation. The continuous Boltzmann equation with a forcing term is given by [31]:

$$\frac{\partial f}{\partial t} + \boldsymbol{\xi} \frac{\partial f}{\partial \boldsymbol{x}} + \frac{\boldsymbol{F}}{\rho} \frac{\partial f}{\partial \boldsymbol{\xi}} = \Omega(f). \tag{2.10}$$

The discretised form of this equation is expressed as:

$$\bar{f}_i(\boldsymbol{x} + \boldsymbol{c}_i \Delta t, t + \Delta t) = \bar{f}_i(\boldsymbol{x}, t) + [\Omega_i(\boldsymbol{x}, t) + S_i(\boldsymbol{x}, t)] \Delta t. \tag{2.11}$$

A full spatial and temporal discretisation of the LBE with forcing, achieving second-order accuracy, is provided by Equation 2.11, where $\bar{f}_i$ is a modified distribution function ensuring second-order accuracy [31]. The modified distribution function is defined as:

$$\bar{f}_i = f_i - \frac{(\Omega_i + S_i)\,\Delta t}{2}. \tag{2.12}$$

When employing the BGK collision operator, the lattice Boltzmann equation simplifies to:

$$\bar{f}_i(\boldsymbol{x} + \boldsymbol{c}_i \Delta t, t + \Delta t) - \bar{f}_i(\boldsymbol{x}, t) = -\frac{\Delta t}{\bar{\tau}} \left(\bar{f}_i - f_i^{\text{eq}} \right) + \left(1 - \frac{\Delta t}{2\bar{\tau}} \right) F_i \Delta t. \tag{2.13}$$

Here, the relaxation parameter is redefined as $\bar{\tau} = \tau + \frac{\Delta t}{2}$ and the source term $S_i = \left(1 - \frac{\Delta t}{2\tau} \right) F_i \Delta t$. The force term F_i will be case-dependent; however, in many multiphase flows, this force term consists of pressure, body, and surface tension forces. For convenience from now onwards, the redefined variables $\bar{f}_i$ and $\bar{\tau}$, will be dropped.

To ensure that the LBE can be solved using a second-order method, the macroscopic velocity must be given by Eq. 2.14, regardless of the forcing scheme. Various forcing schemes exist; however, the most commonly used is the one developed by Guo et al., as they recover the continuity and momentum equations by removing undesired derivatives resulting from time discretisation artefacts [32].

$$\boldsymbol{u} = \frac{1}{\rho} \sum_i \boldsymbol{c}_i f_i + \frac{\boldsymbol{F}\Delta t}{2\rho} \tag{2.14}$$

The equilibrium velocity, using Guo et al.'s proposed method, will assume that $\boldsymbol{u} = \boldsymbol{u}^{eq}$. Additionally, the force term F_i in Eq. 2.13 will be given by Eq. 2.15:

$$F_i = w_i \left(\frac{\boldsymbol{c}_i - \boldsymbol{u}}{c_s^2} + \frac{(\boldsymbol{c}_i \cdot \boldsymbol{u})\,\boldsymbol{c}_i}{c_s^4} \right) \cdot \boldsymbol{F}. \tag{2.15}$$

2.3. Velocity space configurations

The discrete velocities, denoted as c_i, along with their corresponding weighting coefficients w_i, collectively constitute velocity sets represented as $\{c_i, w_i\}$. These velocity sets are conventionally designated as DdQq, where 'd' represents the number of spatial dimensions covered by the velocity set, and 'q' denotes the set's number of velocities.

2.3.1. 1-D Velocity sets

The 1-D lattice configurations for this problem include D1Q2, D1Q3, and D1Q5, as illustrated in Fig. 2.1. Each node within the lattice possesses a unique distribution function and corresponding velocity vectors. Taking D1Q5 as an example, the velocity vectors are c_0, c_1, c_2, c_3 and c_4, while the distribution functions are represented by f_0, f_1, f_2, f_3 and f_4. In LBM simulations it is recommended to discretise both the spatial and temporal dimensions using equal stepping values, denoted as $\Delta x = \Delta t$. In both D1Q3 and D1Q5, the central node (0th) remains stationary with zero velocity, resulting in its distribution function not being involved in the streaming process. The distribution of the central node for higher dimensions (D2 and D3 lattices) is not streamed either.
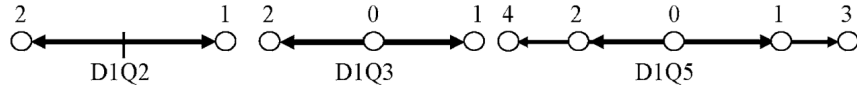
Figure 2.1.: Lattice arrangement for 1-D velocity sets [33].

2.3.2. 2-D Velocity sets

Predominant velocity sets utilized in two-dimensional scenarios encompass D2Q4, D2Q5, and D2Q9. While alternatives like D2Q7 exist, the former configurations hold greater relevance [34]. Figure 2.2 depicts the lattice configurations for D2Q4, D2Q5, and D2Q9, respectively.
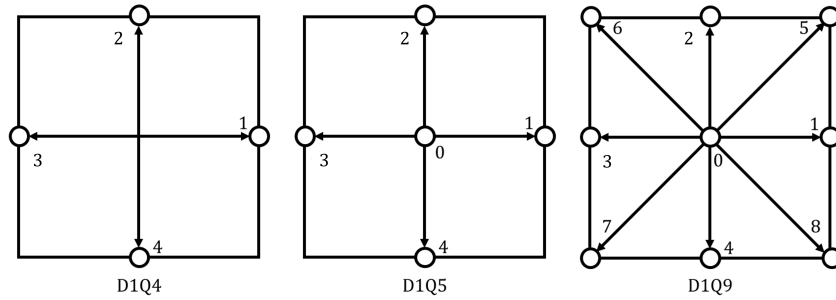
Figure 2.2.: Lattice arrangement for 2-D velocity sets.

D2Q5 and D2Q9 lattice Boltzmann models differ in boundary complexities, with D2Q5 proving more robust for convection-diffusion equations under conditions of weak convection.

The influence of porosity on the performance of different lattice Boltzmann schemes in mass transport simulations showcases greater differences with higher complexity geometries. The D2Q9 outperforms the D2Q4 and D2Q5 lattice configurations [35, 36]. The former aligns with the fact that including more velocity sets utilizes additional distribution functions, ensuring Galilean invariance.

2.3.3. 3-D Velocity sets
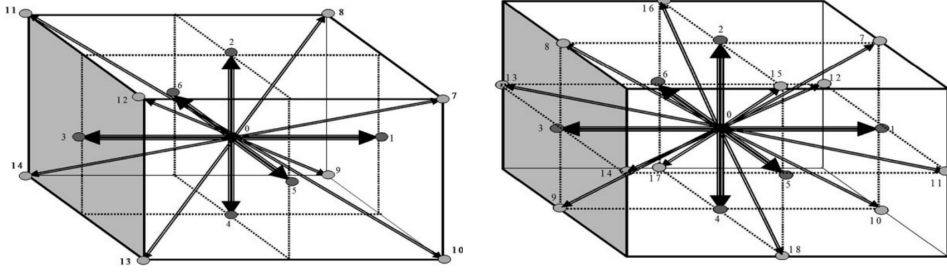
Figure 2.3.: Lattice arrangement for 3-D velocity sets [33].

Fig. 2.3 visually presents prevalent three-dimensional lattice configurations, notably D3Q15 and D3Q19. While lower configurations like D3Q7 and D3Q6 exist, it is recommended to choose at least D3Q15 to maintain system isotropy [31]. Additionally, there are lattice configurations, such as D3Q27, incorporating more distribution functions; however, they tend to be computationally expensive.

The current study will focus mainly in 2D systems however, a 3D case will also be implemented. The velocity sets used will be D2Q9, D3Q7 and D3Q19, which have weights, velocity vectors and speeds of sound shown in Tab. 2.1-2.3, respectively.

Table 2.1.: The D2Q9 velocity set, which has a speed of sound of $c_s = 1/\sqrt{3}$.

i	0	1	2	3	4	5	6	7	8
w_i	$\frac{4}{9}$	$\frac{1}{9}$	$\frac{1}{9}$	$\frac{1}{9}$	$\frac{1}{9}$	$\frac{1}{36}$	$\frac{1}{36}$	$\frac{1}{36}$	$\frac{1}{36}$
c_{ix}	0	+1	0	-1	0	+1	-1	-1	+1
c_{iy}	0	0	+1	0	-1	+1	+1	-1	-1

Table 2.2.: The D3Q7 velocity set, which has a speed of sound of $c_s = 1/2$.

i	0	1	2	3	4	5	6
w_i	$\frac{1}{4}$	$\frac{1}{8}$	$\frac{1}{8}$	$\frac{1}{8}$	$\frac{1}{8}$	$\frac{1}{8}$	$\frac{1}{8}$
c_{ix}	0	+1	-1	0	0	0	0
c_{iy}	0	0	0	+1	-1	0	0
c_{iz}	0	0	0	0	0	+1	-1

Table 2.3.: The D3Q19 velocity set, which has a speed of sound of $c_s = 1/\sqrt{3}$.

i	0	1	2	3	4	5	6	7	8	9	10	11	12	13	14	15	16	17	18
w_i	$\frac{1}{3}$	$\frac{1}{18}$	$\frac{1}{18}$	$\frac{1}{18}$	$\frac{1}{18}$	$\frac{1}{18}$	$\frac{1}{18}$	$\frac{1}{36}$	$\frac{1}{36}$	$\frac{1}{36}$	$\frac{1}{36}$	$\frac{1}{36}$	$\frac{1}{36}$	$\frac{1}{36}$	$\frac{1}{36}$	$\frac{1}{36}$	$\frac{1}{36}$	$\frac{1}{36}$	$\frac{1}{36}$
c_{ix}	0	+1	-1	0	0	0	0	+1	-1	+1	-1	0	0	+1	-1	+1	-1	0	0
c_{iy}	0	0	0	+1	-1	0	0	+1	-1	0	0	+1	-1	-1	+1	0	0	+1	-1
c_{iz}	0	0	0	0	0	+1	-1	0	0	+1	-1	+1	-1	0	0	-1	+1	-1	+1

2.4. Stability

The LBM, like any other numerical scheme, faces two major challenges: numerical stability and accuracy. Instability is typically caused by truncation errors and ill-posed time evolution. The stability of LB simulations hinges on the magnitude of the relaxation factor. In the case of the BGK collision operator, stability depends solely on one relaxation factor, denoted as τ. For the Two Relaxation Time (TRT) collision operator, the stability relies on two relaxation factors, denoted as (τ^+, τ^-). Similarly, for Multiple Relaxation Time (MRT) collision operators with q relaxation times τ_i and a DdQq velocity set [31].

Analysing stability criteria analytically in the bulk, away from boundaries, is a common practice in LB. It is crucial to assess stability on a case-by-case basis for different simulations to ensure adaptability and robustness. The Lattice-BGK (LBGK) stability conditions exhibit four possible behaviours based on the ratio of the relaxation factor to the time step, $\tau/\Delta t$: under-relaxation, over-relaxation, full-relaxation, and instability. Instability occurs when $\tau/\Delta t \leq 1/2$. Under-relaxation happens when $\tau/\Delta t > 1$, causing exponential decay of f_i towards f_i^{eq}, resembling the behaviour in the continuous-time BGK equation. Full relaxation is observed at $\tau/\Delta t = 1$, causing f_i to directly decay to f_i^{eq}. Over-relaxation is evident in the range $1/2 < \tau/\Delta t < 1$, inducing oscillations of f_i around f_i^{eq} with exponentially decreasing amplitude [37]. The three latter cases are represented in Fig. 2.4, where the case when $\tau/\Delta t \leq 1/2$ results in an oscillating increasing exponential distribution function f_i around its equilibrium position f_i^{eq}, increasing exponentially.
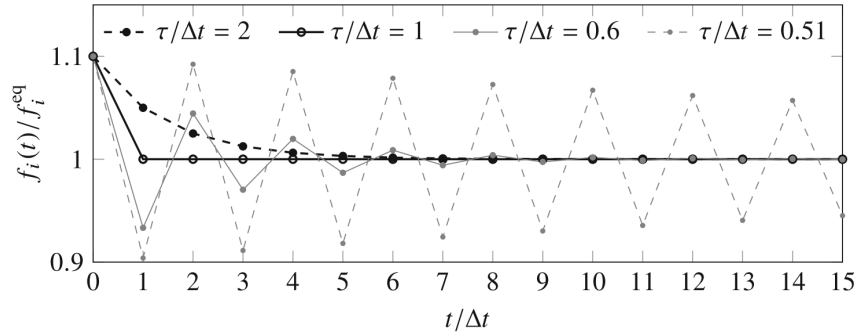
Figure 2.4.: Evolution of the distribution functions for the BGK collision operator for different ratios of $\tau/\Delta t$ [31].

Concerning the BGK collision operator, a sufficient stability condition is when all equilibrium populations remain non-negative. This condition holds true for any τ value where

$\tau/\Delta t > \frac{1}{2}$. Additionally, for the BGK collision operator, an optimal stability condition for the range $\tau/\Delta \geq 1$ is the non-negativity of the rest equilibrium population [37]. The magnitude of the velocity of the simulation can be used to identify stability as well, leading to

$$|u| < \sqrt{\frac{2}{3}} \frac{\Delta x}{\Delta t}. \tag{2.16}$$

For the BGK collision operator, using the conventional definition of the equilibrium distribution population (Eq. 2.6), the maximum allowable velocity magnitude can also serve as a stability condition. The maximum allowable velocity magnitude for different velocity sets is shown in Eq. 2.17,

$$|u_{\max}| < \begin{cases} \sqrt{\frac{2}{3}} \frac{\Delta x}{\Delta t} \approx 0.816 \frac{\Delta x}{\Delta t} & \text{for D1Q3} \\ \sqrt{\frac{1}{3}} \frac{\Delta x}{\Delta t} \approx 0.577 \frac{\Delta x}{\Delta t} & \text{for D2Q9, D3Q15, D3Q19, D3Q27} \end{cases}. \tag{2.17}$$

Analytical results can be obtained for the bulk LBE of a flow that provides stability, as depicted in Fig. 2.5a. LBM simulations, which include boundaries, may encounter stability issues when $|u_{\max}| \to 0$ with the viscosity also going to zero. This issue is identified through linear stability analysis (von Neumann Analysis) or the non-negativity of the discrete distribution functions f_i [37]. Niu et al. [38] conducted von Neumann linearised stability analysis under a uniform flow condition for an LBM simulation with a D2Q9 velocity set. They found that the maximum velocity is related to the relaxation time via Eq. 2.18, as illustrated in Fig. 2.5b. However, this relation does not hold for any flow, as it heavily depends on the boundary conditions of the analysed problem.

$$|u_{\max}|(\tau) < \begin{cases} 8\left(\frac{\tau}{\Delta t} - \frac{1}{2}\right)\frac{\Delta x}{\Delta t} & \text{for } \frac{\tau}{\Delta t} < 0.55 \\ 0.4\frac{\Delta x}{\Delta t} & \text{for } \frac{\tau}{\Delta t} \geq 0.55. \end{cases} \tag{2.18}$$
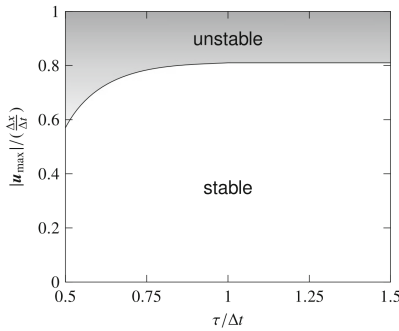
(a) Sketch of the analytical sufficient and optimal stability regions for 2D and 3D simulations [31].
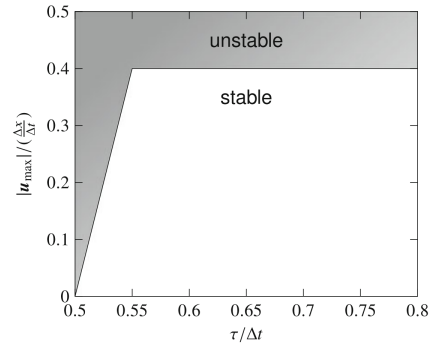
(b) Stability regions for a D2Q9 velocity set, analyzed via a Von Neuman linear stability by Niu et al [31, 38].

Figure 2.5.: Stability for LBM.

2.5. MRT collision operator

The fundamental concept behind the Multiple-Relaxation-Time (MRT) collision operator is the transformation of the distribution functions (populations) into moment space using a transformation matrix $\boldsymbol{M}$. This approach enables the relaxation of moments, rather than populations, at distinct rates governed by a relaxation matrix $\boldsymbol{S}$. After the moments are relaxed, they are transformed into population space, where the standard streaming process is applied; mathematically, this means that

$$\boldsymbol{f}\left(\boldsymbol{x}+\boldsymbol{c}_i\Delta t, t+\Delta t\right) = \boldsymbol{f}(\boldsymbol{x},t) - \boldsymbol{M}^{-1}\boldsymbol{S}\boldsymbol{M}\left[\boldsymbol{f}(\boldsymbol{x},t) - \boldsymbol{f}^{\text{eq}}(\boldsymbol{x},t)\right]\Delta t. \tag{2.19}$$

The process to employ an MRT collision operator is to first compute the conserved moments—density ρ and momentum $\boldsymbol{j} = \rho\boldsymbol{u}$— from the pre-collision distribution functions. These are obtained through the following expressions:

$$\rho = \sum_i f_i, \quad \rho\boldsymbol{u} = \sum_i f_i\boldsymbol{c}_i. \tag{2.20}$$

After determining the conserved moments, the next step involves transforming the distribution functions f_i into moment space. This is achieved using a transformation matrix $\boldsymbol{M}$, leading to the calculation of the moments m_k, where k represents the moment, as,

$$\boldsymbol{m} = \boldsymbol{M}\boldsymbol{f}, \quad m_k = \sum_i M_{ki}f_i. \tag{2.21}$$

With the moments in hand, the equilibrium moments $\boldsymbol{m}^{\text{eq}}$ are computed. These can either be directly obtained from the relation $\boldsymbol{m}^{\text{eq}} = \boldsymbol{M}\boldsymbol{f}^{\text{eq}}$ or more precisely constructed from the known conserved quantities ρ and $\rho\boldsymbol{u}$ using a general polynomial representation:

$$m_k^{\text{eq}} = \rho \sum_{l,m,n} a_{k,lmn}u_x^l u_y^m u_z^n. \tag{2.22}$$

The coefficients $a_{k,lmn}$ used in this polynomial representation can be determined using approaches such as the Hermite polynomial or the Gram-Schmidt orthogonalization. Once both the moments $\boldsymbol{m}$ and their equilibrium counterparts $\boldsymbol{m}^{\text{eq}}$ are available, the collision step is performed in moment space. This involves relaxing the moments toward their equilibrium values according to the BGK-type relaxation:

$$m_k^* = m_k - \omega_k\left(m_k - m_k^{\text{eq}}\right)\Delta t. \tag{2.23}$$

It is important to note that during this collision process, the conserved moments ρ and $\boldsymbol{j}$ remain unchanged, except in cases where external forces or sources are present. After the collision, the post-collision distribution functions $f_i^\star$ are reconstructed by transforming the moments back to population space using the inverse of the transformation matrix:

$$f_i^\star = \sum_k M_{ik}^{-1}m_k^*. \tag{2.24}$$

Finally, the process concludes with the streaming step, where the populations are advected according to the LBM algorithm. The MRT collision operator, briefly described above, shows how it handles different relaxation rates for different physical quantities, enhancing stability and accuracy in lattice Boltzmann simulations.

2.6. Boundary Conditions

In conventional numerical methods, boundary conditions are typically known and applied at their corresponding geometrical locations. Consider a planar Couette flow as an example. To generate a numerical solution for this flow, two boundary conditions are required. Both of these boundary conditions are always no-slip conditions to ensure that the discretized elements touching the plate move with the same velocity as the plate, regardless of whether the plate has velocity or not.

In LBE simulations, boundary conditions are applied at boundary nodes $(\boldsymbol{x}_b)$, which are nodes that connect the fluid and solid nodes. Specifying boundary conditions in LBE simulations is a non-trivial task, as it involves applying relevant conditions to the mesoscopic populations (f_i), which have higher degrees of freedom. There are three general types in which boundary conditions are applied: Dirichlet, Neumann, and Robin (or mixed) boundary conditions.

2.6.1. Dirichlet boundary condition

The classical mathematical definition of a Dirichlet boundary condition is a specific value that the solution of a differential equation should take along a boundary. In LBE, this is also the case; however, the value being specified is directly related to the mesoscopic populations. For a 1-D problem using D1Q2 or D1Q3, with a known scalar φ, the boundary condition can be defined as:

$$\varphi = f_1 + f_2. \tag{2.25}$$

At the left-hand side of the domain, the value of f_2 is obtained from the streaming process, leaving f_1 as the only unknown [33]. Alternatively, a detailed flux balance can be realized at the boundary, as follows (only shown for D1Q2):

$$f_1^{eq} - f_1 + f_2^{eq} - f_2 = 0. \tag{2.26}$$

By rearranging the equation, the value of f_1 can be found using the definition of the equilibrium distribution function:

$$f_1 = f_1^{eq} + f_2^{eq} - f_2. \tag{2.27}$$

The previous explanation was shown for 1-D problems, but the same logic applies to higher dimensions. In cases where there are diagonal distribution functions, such as in the D2Q9 velocity sets, there will be more unknowns. The distribution populations f_5 and f_8 will also be unknowns, found with their outward inverse streaming distribution functions f_7 and f_6, respectively, and their equilibrium distribution functions.

2.6.2. Neumann boundary condition

A Neumann boundary condition specifies the value of the derivative of a differential equation (Eq. 2.28), where α is a coefficient. To translate this into LB simulations, the derivative of the equation is discretised.

$$\frac{\partial \varphi}{\partial x} = \alpha. \tag{2.28}$$

Taking a known scalar in a 1-D problem using a D1Q2 velocity set, a Neumann boundary condition is employed as seen below:

$$\frac{\varphi(i+1) - \varphi(i)}{\Delta x} = \alpha. \tag{2.29}$$

Knowing that $\varphi = f_1 + f_2$:

$$f_1(i) + f_2(i) + \alpha \Delta x = f_1(i+1) + f_2(i+1). \tag{2.30}$$

By equating the distribution functions and splitting the coefficient equally, it is rational to assume that $f_1(i) = f_1(i+1) - \alpha \Delta x/2$ and $f_2(i) = f_2(i+1) - \alpha \Delta x/2$. Once again, this procedure also applies to higher dimensions.

2.6.3. Robin boundary condition

A Robin boundary condition is a specification of a linear combination of the values of a function and the values of its derivative at the boundary. The generic form of a Robin boundary condition is:

$$\frac{\partial \varphi}{\partial x} = a\varphi + b. \tag{2.31}$$

For a D1Q2 velocity set with a flux in the positive x-direction, the unknown distribution function will be:

$$f_1 - f_2 = a(f_1 + f_2) + b, \tag{2.32}$$

$$f_1 = \frac{f_2(1+a) + b}{1 - a}, \ a \neq 1. \tag{2.33}$$

It is essential to perform a proper conversion of physical space parameters to lattice space. The relaxation parameter, or multiple relaxation parameters, and the distribution functions are modeled from the macroscopic equation that describes the physics. In LB, the Chapman-Enskog analysis is used to derive the relation of the macroscopic transport properties and the simulation parameters.

3. Multiphase flows in LBM

The LBM has experienced significant success in simulating single-phase flows over the past few decades. In recent years, there has been a notable surge in the development of multiphase LBM, resulting in various approaches to analysing multiphase flows. LBM's popularity in simulating multiphase and multicomponent flows can be attributed to its ability to automatically maintain sharp interfaces, eliminating the need for explicit interface tracking [34].

Numerous LBM models have been proposed for multiphase and multicomponent problems. The colour-gradient model, also known as the RK model, represents the pioneering model based on the Rothman-Keller multiphase lattice gas model [39]. Subsequently, the Shan-Chen pseudopotential model emerged, incorporating attractive or repulsive forces that induce phase separation [40]. The Free-energy and Interface tracking models followed suit (HZC) [1, 41]. The upcoming chapter will offer an introduction and assessment of the Shan-Chen, Colour Gradient and Interface Tracking model. The assestment will be done by analysing a static bubble scenario and comparing the results of each method with analytical results. On the basis of this comparison, an appropriate multiphase model will be chosen to simulate bubble growth through further development.

3.1. Shan-Chen (SC) Pseudopotential model

The Shan-Chen (SC) pseudopotential method is a bottom-up approach, where the microscopic interactions between fluid elements are postulated first, and then the macroscopic interactions. The intrinsic simplicity and mesoscopic approach of the SC model are its main advantages. In the SCMP system, the SC model incorporates a forcing term in the LBE by replacing the ideal gas equations of state in the single-phase LBM with a non-ideal, non-monotonic equation of state. Meanwhile, in the MCMP model, each component is represented by its distribution function. The key idea behind the SC model is the addition of a simple interaction force at the nodes.

It is reasonable to assume that intermolecular forces act pairwise and are cumulative. The strength of the interaction between fluid elements at x and $\tilde{x} \neq x$ is proportional to $\rho(x)\rho(\tilde{x})$. This interaction is also influenced by the spatial separation between the fluid elements, introducing a kernel function $G(x, \tilde{x})$ to encapsulate the spatial dependence of the force [31]. The discretized interaction force density at x for multicomponent, multiphase systems can be written as

$$\mathbf{F}^{\mathrm{SC}(k)}(x) = -\psi^{(k)}(x) \sum_{\tilde{k}} G_{k\tilde{k}} \sum_{i} w_i \psi^{(\tilde{k})}\left(x + \mathbf{c}_i \Delta t\right) \mathbf{c}_i \Delta t. \tag{3.1}$$

In Eq. 3.1, we can have different components k, ranging up to S components. For this model, the sum is over all pseudopotential interactions between the nearest lattice neighbors within

the same fluid and for other components. Here, $G_{k\tilde{k}}$ is a scalar denoting the strength of the molecular interaction between different fluid components, and $\psi(\rho)$ is the pseudopotential, used instead of density for greater numerical stability. Shan and Chen used Eq.3.2 as the pseudopotential function, where ρ_0 is a reference density that, in most simulations, is set to unity [40, 42],

$$\psi(\rho) = \rho_0 \left[1 - \exp(-\rho/\rho_0)\right]. \tag{3.2}$$

To implement an LB simulation using the MCMP Shan-Chen model, changes are made to the LBM. The distribution function for the kth fluid using the BGK collision operator is given by Eq. 3.3:

$$f_i^k \left(\boldsymbol{x} + \boldsymbol{c}_i \Delta t, t + \Delta t\right) = f_i^k(\boldsymbol{x}, t) - \frac{1}{\tau_k} \left[f_i^k(\boldsymbol{x}, t) - f_i^{k,eq}(\boldsymbol{x}, t)\right], \tag{3.3}$$

where the equilibrium distribution function $(f_i^{k,eq})$ is expressed as:

$$f_i^{k,eq} = w_i \rho_k \left[1 + \frac{\boldsymbol{c}_i \cdot \boldsymbol{u}^{k,eq}}{c_s^2} + \frac{\left(\boldsymbol{c}_i \cdot \boldsymbol{u}^{k,eq}\right)^2}{2c_s^4} - \frac{\left(\boldsymbol{u}^{k,eq}\right)^2}{2c_s^2}\right]. \tag{3.4}$$

The individual macroscopic density ρ_k and momentum $\rho_k \boldsymbol{u}_k$ for the kth fluid are defined as $\sum_i f_i^k$ and $\sum_i f_i^k \boldsymbol{c}_i$, respectively (its zeroth and first-order moments). The velocity of each component will be given by,

$$\boldsymbol{u}^{k,eq} = \boldsymbol{u}' + \frac{\tau_k \boldsymbol{F}^{\text{SC}(k)}}{\rho_k} \tag{3.5}$$

where $\boldsymbol{u}'$ is a common velocity to conserve momentum given by Eq.3.6, and $\boldsymbol{F}^{\text{SC}(k)}$ is the net force, accounting for both fluid-fluid cohesion $\boldsymbol{F}^{k,ff}$ and fluid-solid adhesion $\boldsymbol{F}^{k,fs}$.

$$\boldsymbol{u}' = \frac{\sum_k \frac{\rho_k \boldsymbol{u}^{(k)}}{\tau_k}}{\sum_k \frac{\rho_k}{\tau_k}}. \tag{3.6}$$

To implement fluid-fluid cohesion interactions, the nearest lattice nodes are used, being described as:

$$\boldsymbol{F}^{k,ff}(\boldsymbol{x}, t) = -G_c \psi_k(\boldsymbol{x}, t) \sum_i w_i \psi_{\tilde{k}} \left(\boldsymbol{x} + \boldsymbol{c}_i \Delta t, t\right) \boldsymbol{c}_i, \tag{3.7}$$

where G_c controls the cohesive force. Repulsive interactions between components $(G_c > 0)$ model partly miscible or immiscible fluid mixtures. This approach has been shown to be equivalent to adjusting the system's free energy explicitly [43]. Additionally, a force exerted by a surface interaction can be introduced as shown in Eq. 3.8,

$$\boldsymbol{F}^{k,fs}(\boldsymbol{x}, t) = -G_{ads,k} \psi_k(\boldsymbol{x}, t) \sum_i w_i s \left(\boldsymbol{x} + \boldsymbol{c}_i \Delta t\right) \boldsymbol{c}_i. \tag{3.8}$$

$G_{ads,k}$ represents the strength of interaction between fluid k and the solid. Note that for this case, $s\left(\boldsymbol{x} + \boldsymbol{c}_i \Delta t\right)$ is an indicator function that will be equal to 0 or 1 depending on whether it is a fluid or solid node respectively.

Given that there is more than one set of populations, it is not immediately clear which velocity $\boldsymbol{u}^{k,eq}$ to use for the equilibrium distribution to find the macroscopic components. The bulk velocity of the fluid is defined by Eq. 3.9, which includes the effect of the interactive force [44]:

$$\boldsymbol{u}_{\mathrm{b}} = \frac{1}{\rho} \sum_k \left(\sum_i f_i^k \boldsymbol{c}_i + \frac{\boldsymbol{F}^{\mathrm{SC}(k)} \Delta t}{2} \right). \tag{3.9}$$

SC Validation

The formulation of the SC, RK and HZC models will be for an SCMP system and implemented in Python. All the simulations will use a D2Q9 velocity set, with a domain size of $N_x = N_y = 100$ lu, where $\Delta x = \Delta y = 1$ lu. Additionally, the bubble for the three models will be initialised with a radius of 20 lu, and have a sharp interface. The simulation is left to iterate for 100,000 iterations or until the maximum difference between the distribution functions (tolerance) is less than 10^{-10}, deemed sufficient conditions for convergence. The edges of the domain are considered as periodic. Lastly, for the SC implementation, a BGK collision operator is used to carry out the relaxation.

The SC model for SCMP systems is highly dependent on $G_{k\tilde{k}}$, which controls the interparticle force, resembling a temperature-like dependence for SCMP systems. Both Krüger et al. and Datadien [20] show the dependence of the density ratio on the value of $G_{k\tilde{k}}$. Figure 3.1 shows that the implementation of the SC model in the present work is accurate as the density ratio dependence matches the results obtained by Datadien for the same test case. Additionally, it can be observed that the SC implementation can achieve density ratios (ρ_1/ρ_g) of up to $O(10^2)$ for the current implementation with lower values of $G_{k\tilde{k}}$.
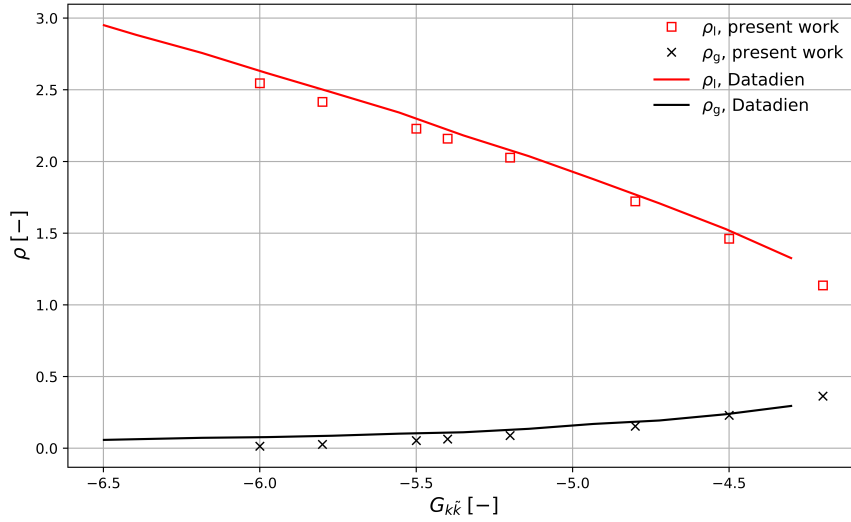
Figure 3.1.: Non-dimensionalised density of the fluid (red) and gaseous (black) phases of an SCMP system. [20, 31].

3.2. Colour-gradient (RK) model

The Rothman–Keller (RK) model is a two-component model, where, historically, one component is the blue coloured fluid and the other is the red colour fluid. Two distribution functions are used to represent the fluids. This model modifies the LBM by an additional collision term and a re-colouring step. Given the two distribution functions, this allows the colour-gradient method to independently adjust the surface tension and the ratio of the viscosities. The RK model has one major drawback: it is limited in its ability to achieve stable density ratios for dynamics simulation, i.e., a moving interface. To increase stability for dynamic simulations, a modified RK model called the RK model with enhanced equilibrium is proposed. This model follows the same logic as the traditional RK model. However, according to Leclaire et al. [45] and Datadien, the distribution function and the collision operator are modified as shown in Eq. 3.10 and Eq. 3.11,

$$f_i^k(\mathbf{x} + \mathbf{c}, t) = f_i^k(\mathbf{x}, t) + \Omega_i^k\left(f_i^k(\mathbf{x}, t)\right), \tag{3.10}$$

$$\Omega_i^k = \left(\Omega_i^k\right)^{(3)}\left[\left(\Omega_i^k\right)^{(1)} + \left(\Omega_i^k\right)^{(2)}\right]. \tag{3.11}$$

Here k can either be R for the red fluid and B for the blue fluid region. The total particle distribution function will be the addition of these two.

$$f_i(\mathbf{x}, t) = f_i^R(\mathbf{x}, t) + f_i^B(\mathbf{x}, t) \tag{3.12}$$

The collision operator depends on three sub-operators, which must be applied sequentially to the distribution function. The three steps are the single-phase collision, a perturbation, and a recolouring step denoted by Eq. 3.13, 3.14, and 3.15, respectively,

$$f_i^k\left(\mathbf{x}, t'\right) = \left(\Omega_i^k\right)^1\left(f_i^k(\mathbf{x}, t)\right), \tag{3.13}$$

$$f_i^k\left(\mathbf{x}, t''\right) = \left(\Omega_i^k\right)^2\left(f_i^k(\mathbf{x}, t')\right), \tag{3.14}$$

$$f_i^k\left(\mathbf{x}, t'''\right) = \left(\Omega_i^k\right)^3\left(f_i^k(\mathbf{x}, t'')\right). \tag{3.15}$$

The collision operator for both fluids, $\left(\Omega_i^k\right)^1$, will be carried out using a single relaxation time (SRT), which takes an identical form for each fluid like Eq 2.4. The equilibrium distribution function is modified to enhance the dynamical stability of the method[45], given by:

$$\begin{aligned} f_i^{k,eq}\left(\rho_k, \mathbf{u}, \alpha_k\right) &= \bar{\nu}\left[\psi_i\left(\mathbf{u} \cdot \nabla \rho_k\right) + \xi_i\left(\mathbf{G}_k : \mathbf{c}_{i,k} \otimes \mathbf{c}_i\right)\right] + \\ &\quad \rho_k\left(C_i + w_i\left[\frac{\mathbf{u} \cdot \mathbf{c}_i}{c_s^2} + \frac{(\mathbf{u} \cdot \mathbf{c}_i)^2}{2c_s^4} - \frac{\mathbf{u} \cdot \mathbf{u}}{2c_s^2}\right]\right), \end{aligned} \tag{3.16}$$

where $C_{i,k}$ accounts for the density difference in k^{th}, which for a D2Q9 velocity set is given by Eq. 3.17,

$$C_{i,k} = \begin{cases} \alpha_k, & i = 0, \\ \frac{1-\alpha_k}{5}, & i = 1,2,3,4 \\ \frac{1-\alpha_k}{20}, & i = 5,6,7,8, \end{cases} \tag{3.17}$$

and α_k is a free parameters that affects the density of the fluids as,

$$\kappa = \frac{\rho_R}{\rho_B} = \frac{1-\alpha_B}{1-\alpha_R}. \tag{3.18}$$

In the modified equilibrium distribution function ψ_i and ξ_i are weights depending on the chosen velocity set, which can be found in literature [45]. The tensor $\boldsymbol{G}_k$ is defined as:

$$\boldsymbol{G}_k = (\boldsymbol{u} \otimes \nabla \rho_k) + (\boldsymbol{u} \otimes \nabla \rho_k)^\top. \tag{3.19}$$

The perturbation operator $\left(\Omega_i^k\right)^2$, takes the form given by Eq. 3.20, imposes surface tension by,

$$\left(\Omega_i^k\right)^2 = f_i^k\left(\boldsymbol{x}, t'\right) + \frac{A_k}{2} |\nabla \phi| \left[w_i \frac{(\boldsymbol{c}_i \cdot \nabla \phi)^2}{|\nabla \phi|^2} - B_i \right], \tag{3.20}$$

where A_k is a tuning parameter that can be set by imposing surface tension as,

$$\sigma = \frac{4A_k}{9\omega_{eff}}, \tag{3.21}$$

where the effective relaxation parameter ω_{eff} is a function of the kinematic viscosity at the interface $\bar{\nu}$, where both parameters are found as,

$$\omega_{\text{eff}} = \frac{2}{6\bar{\nu}+1}, \tag{3.22}$$

$$\frac{1}{\bar{\nu}} = \frac{\rho_R}{\rho_R + \rho_B} \frac{1}{\nu_R} + \frac{\rho_B}{\rho_R + \rho_B} \frac{1}{\nu_B}. \tag{3.23}$$

Additionally in Eq. 3.20, B_i are constant for each distribution and their values will depend on the velocity set chosen. For a D2Q9 velocity set the values of B_i are $B_0 = -\frac{4}{27}, B_i = \frac{2}{27}$ for $i = 1,2,3,4$, and $B_i = \frac{5}{108}$ for $i = 5,6,7,8$. Lastly, ϕ is the phase field which is computed with Eq. 3.24,

$$\phi(\boldsymbol{x}) = \frac{\rho_R(\boldsymbol{x}) - \rho_B(\boldsymbol{x})}{\rho_R(\boldsymbol{x}) + \rho_B(\boldsymbol{x})}, \tag{3.24}$$

This implies that $|\phi| \leq 1$, and that $\phi = 1$ is a purely red fluid region and $\phi = -1$ is a purely blue fluid region. The gradient of the phase field $\nabla \phi$, is determined with a fourth-order-accurate isotropic finite difference scheme[46, 47],

$$\nabla \phi = \frac{1}{c_s^2 \Delta t} \sum_i w_i \boldsymbol{c}_i \phi(\boldsymbol{x} + \boldsymbol{c}_i, t). \tag{3.25}$$

The recolouring operator, $\left(\Omega_i^k\right)^3$, implemented by Latva-Kokko and Rothman to achieve phase separation and maintain the sharpness of the interface modifies the post-collision distribution functions as:

$$\left(\Omega_i^R\right)^3 = \frac{\rho_R}{\rho} f_i^* + \beta \frac{\rho_R \rho_B}{\rho^2} f_i^{(eq)}(\rho, \boldsymbol{u} = 0) \cos(\varphi_i),$$
$$\left(\Omega_i^B\right)^3 = \frac{\rho_B}{\rho} f_i^* - \beta \frac{\rho_R \rho_B}{\rho^2} f_i^{(eq)}(\rho, \boldsymbol{u} = 0) \cos(\varphi_i),$$

(3.26)

where β is the separation parameter, which can take a value between 0 and 1, and φ is the angle between the phase field and the lattice velocity vector as 3.27,

$$\cos(\varphi_i) = \frac{\boldsymbol{c}_i \cdot \boldsymbol{\phi}}{|\boldsymbol{c}_i| \cdot |\boldsymbol{\phi}|}.$$

(3.27)

Additionally, in Eq. 3.26, $f_i^* = \sum_k f_i^{k*}$. After the recolouring step, the particle distribution functions stream to the neighboring lattice by,

$$f_i^k(\boldsymbol{x} + \boldsymbol{c}_i \Delta t, t + \Delta t) = f_i^{k,+}(\boldsymbol{x}, t).$$

(3.28)

The density per component, the total density, and the momentum are determined respectively by, respectively,

$$\rho_k = \sum_i f_i^k,$$

(3.29)

$$\rho = \sum_k \rho_k,$$

(3.30)

$$\rho \boldsymbol{u} = \sum_k \sum_i f_i^k \boldsymbol{c}_i.$$

(3.31)

RK Validation

To validate the RK-enhanced equilibria model for a static bubble, the Laplace law can be used to determine the pressure jump analytically as,

$$\Delta p = \frac{\sigma}{R},$$

(3.32)

where σ is the surface tension and R is the radius of the bubble. The analytical values can then be compared with Eq. 3.33, which determines the pressure difference across the bubble interface in the simulation.

$$p_k = \eta(1 - \alpha_k)\rho_k$$

(3.33)

In Eq. 3.33, η will be a parameter dependent on the velocity set used, where for the D2Q9 case, $\eta = 3/5$. The tunable parameter $\beta = 0.7$ will reduce the interface thickness as much as possible, and the density ratio will have a value of $\rho_R/\rho_B = 10$ and will remain constant for the validation. As all other parameters in a LBM simulation, surface tension will

be dimensionless lattice units. The corresponding lattice units of σ are mu/tu^2, where the numerator is mass units and the denominator is time units. The relationship between pressure difference, surface tension, and radius of the bubble is plotted in Figure 3.2a, which is consistent with the Laplace law. For small bubble radii, $R \leq 15$, the relative deviation is more significant than 15% as the interface width becomes almost the same size as the radius (w $\approx$ 7 lu). Additionally, as the surface tension increases, so does the relative error $\delta_{\sigma} = (\sigma - \sigma_{\text{num}}) / \sigma \times 100$, as shown in Figure. 3.2b This occurs as the immiscibility between the fluids increases and the artificial forces acting around the interface increase, generating more pronounced spurious velocities.

3.3. Interface Tracking and Mass Transfer Across the Interface

In the interface tracking model, also known as the He-Chen-Zhang (HCZ) model, interfacial dynamics are modelled by incorporating molecular interactions, which are done by introducing two distribution functions: one for the pressure and, another generally, for the order parameter. These will recover the N-S and Cahn-Hilliard (CH) interface tracking equations. However, using the CH equation causes tiny droplets to disappear once their radius falls below a critical value [1]. Additionally, as the CH equation involves the Laplacian of the order parameter, 4$^{\text{th}}$-order derivatives have to be calculated to compute the chemical potential. Consequently, another class of interface tracking was proposed, called the phase-field equation, where, at maximum, 2$^{\text{nd}}$-order derivatives would need to be determined. The primary advantage of the HCZ model proposed by Fakhari et al. [48] is that it was later modified by Tan et al. to incorporate a mass flux term between two phases. The following sub-section will describe the LBM proposed by Tan et al., Fakhari et al..

Phase-Field evolution equations

According to Fakhari et al., the conservative phase-field (ϕ) in an incompressible two-phase flow reads as:

$$\frac{\partial \phi}{\partial t} + \nabla \cdot (\boldsymbol{u}\phi) = \nabla \cdot \left\{ M \left[\nabla \phi - \frac{1 - 4\left(\phi - \phi_{\text{avg}}\right)^2}{W} \boldsymbol{n} \right] \right\} + \frac{\dot{m}}{\rho_l}, \tag{3.34}$$

where W is the width of interface, M is the mobility of the interface, $\phi_{\text{avg}} = \left(\phi_l + \phi_g\right)/2 = 0.5$ is always used to indicate the location of the interface, $\boldsymbol{n} = (\nabla \phi)/|\nabla \phi|$ is the unit vector normal to the interface. The last term in Eq. 3.34 is a source term that will account for species transfer across the interface. To couple the phase-field method with the concentration evolution, Tan et al. made four assumptions: the bubble is filled by a single component with constant concentration, the concentration field is considered as a passive scalar, there are no temperature gradients in the system, and at the interface Henry's Law is assumed for the mass transfer phenomena.

Diffusion mechanisms are responsible for the mass transfer rate and volume change for the different phases. For continuous species transfer, the velocity near the interface $\boldsymbol{u}_l$ and the

concentration gradients will be the principal reasons why the mass flux q across the interface varies. According to Maes and Soulaine, the mass flux will be given by:

$$q = \begin{cases} -D_{\text{eff}}\,\nabla C + D_{\text{eff}}\,\frac{1-He}{\phi+(1-\phi)He}C\nabla\phi & \boldsymbol{u}_l = \boldsymbol{0}, \\ -\frac{D_{\text{eff}}\,\nabla C + D_{\text{eff}}^{\phi+(1-\phi)He}C\nabla\phi}{\phi} & \boldsymbol{u}_l \neq \boldsymbol{0}. \end{cases} \tag{3.35}$$

where C is the concentration mixture of the multicomponent/multiphase system, D_{eff} is the harmonic mean diffusion coefficient averaged between the different phases, given respectively by:

$$C = \phi C_l + (1-\phi)C_g, \tag{3.36}$$

$$D_{eff} = \frac{D_l D_g}{D_l(1-\phi) + D_g\phi}. \tag{3.37}$$

Additionally, He is the distribution coefficient at the interface, which Henry's Law gives as the ratio of the gaseous to liquid concentration (i.e., $He = C_g/C_l$). This value is constant and for the system in question. For AWE at $80°C$, it will have a value of $He \approx 309.82$ [50]. The source term can be found as the integral of the mass flux over the interface:

$$\dot{m} = \int_S (q \cdot \boldsymbol{n})dS = \int_\Omega (q \cdot \boldsymbol{n}|\nabla\phi|)d\Omega = \int_\Omega (q \cdot \nabla\phi)d\Omega, \tag{3.38}$$

where S is the interfacial area and Ω the control volume. As the control volume in lattice units is one, the value through which the integral is realised becomes one, thus substituting Eq.3.38 into Eq.3.34 the phase field equation becomes:

$$\frac{\partial\phi}{\partial t} + \nabla \cdot (\boldsymbol{u}\phi) = \nabla \cdot \left\{ M \left[\nabla\phi - \frac{1-4\left(\phi-\phi_{\text{avg}}\right)^2}{W}\boldsymbol{n} \right] \right\} + \frac{q \cdot \nabla\phi}{\rho_l}. \tag{3.39}$$

As the LBE equation is inherently conservative, the phase field equation can be solved by applying the collision and streaming operation of the LBM as shown by Eq.3.40 and Eq.3.41.

$$\hat{g}_i(\boldsymbol{x},t) = g_i(\boldsymbol{x},t) - \frac{g_i(\boldsymbol{x},t) - g_i^{\text{eq}}(\boldsymbol{x},t)}{\tau_\phi + 0.5} \tag{3.40}$$

$$g_i\left(\boldsymbol{x} + \boldsymbol{c}_i\Delta t, t + \Delta t\right) = \hat{g}_i(\boldsymbol{x},t) \tag{3.41}$$

In the previous equations, τ_ϕ is the relaxation time given by $\tau_\phi = M/(c_s^2\Delta t)$, where M is the mobility which is a tuning parameter. The equilibrium distribution $g_i^{\text{eq}}(\boldsymbol{x},t)$ will be determined as Tan et al. proposes:

$$g_i^{\text{eq}}(\boldsymbol{x},t) = \omega_i\phi\left[1 + \frac{\boldsymbol{c}_i \cdot \boldsymbol{u}}{c_s^2} + \frac{(\boldsymbol{c}_i \cdot \boldsymbol{u})^2}{2c_s^4} - \frac{\boldsymbol{u} \cdot \boldsymbol{u}}{2c_s^2}\right] + \frac{M}{c_s^2}\left[\frac{1-4\left(\phi-\phi_{\text{avg}}\right)^2}{W}\right]\omega_i\boldsymbol{c}_i \cdot \boldsymbol{n}. \tag{3.42}$$

The second term on the right-hand side is introduced to appropriately modify the flux at the interface, ensuring the interface is as sharp as possible. The zeroth order macroscopic component that is recovered is the Phase Field, as shown by,

$$\phi = \sum_i g_i, \tag{3.43}$$

However, to ensure that the mass source is recovered with a second-order accuracy we first define the population sources as

$$Q_i = w_i q. \tag{3.44}$$

Performing a Chapman-Enskog analysis with the additional terms Q_i, we find that the macroscopic Advection Diffusion Equation (ADE) becomes

$$\frac{\partial \phi}{\partial t} + \nabla \cdot (\boldsymbol{u}\phi) = \nabla \cdot \left\{ M \left[\nabla \phi - \frac{1 - 4(\phi - \phi_{\text{avg}})^2}{W} \boldsymbol{n} \right] \right\} + \frac{\dot{m}}{\rho_l} - \frac{\Delta t}{2} \frac{\partial q}{\partial t}. \tag{3.45}$$

To remove the unphysical $-\frac{\Delta t}{2}\frac{\partial q}{\partial t}$ term, the relaxation time is redefined as $\overline{\tau}_\phi = \tau_\phi + \Delta t/2$, which then redefines the macroscopic moments as,

$$\phi = \sum_i g_i + \frac{Q_i \Delta t}{2}, \quad Q_i = \left(1 - \frac{1}{2\overline{\tau}_\phi}\right) w_i q. \tag{3.46}$$

It is worth noting that the redefined relaxation time should also be used in the collision step, Eq. 3.40.

Concentration evolution equation

The phase field is a diffuse interface model, where the interface between components/phases contains a designated number of grid points over which the physical properties change smoothly. A single-field approach can be adopted in which the unified concentration equation of the different species is established by a conditional volume average technique [19]. At the interface, it is considered that there is thermodynamic equilibrium, and thus the concentration equation will be governed by:

$$\frac{\partial C}{\partial t} + \boldsymbol{u} \cdot \nabla C = \nabla \cdot (D_{\text{eff}} \nabla C) - \nabla \cdot \left[D_{\text{eff}} \frac{1 - He}{\phi + (1 - \phi)He} C \nabla \phi \right]. \tag{3.47}$$

The distribution function corresponding to the ADE for concentration proposed by Tan et al. can then be expressed as:

$$h_i(\boldsymbol{x} + \boldsymbol{c}_i \Delta t, t + \Delta t) = h_i(\boldsymbol{x}, t) - \frac{1}{\tau_h} \left[h_i(\boldsymbol{x}, t) - h_i^{\text{eq}}(\boldsymbol{x}, t) \right], \tag{3.48}$$

where τ_h is the relaxation time and $h_i^{\text{eq}}(\boldsymbol{x}, t)$ is given by,

$$h_i^{\text{eq}}(\boldsymbol{x}, t) = \omega_i C \left[1 + \frac{\boldsymbol{c}_i \cdot \boldsymbol{u}}{c_s^2} + \frac{(\boldsymbol{c}_i \cdot \boldsymbol{u})^2}{2c_s^4} - \frac{\boldsymbol{u} \cdot \boldsymbol{u}}{2c_s^2} \right] + \frac{D_{\text{eff}}}{c_s^2} \left[\frac{1 - He}{\phi + (1 - \phi)He} C |\nabla \phi| \right] \omega_i \boldsymbol{c}_i \cdot \boldsymbol{n}. \tag{3.49}$$

However, to enhance the stability of the system and allow a greater range of values of diffusivities to be used, an MRT collision operator will be proposed in the present study. Thus, Eq. 3.48 will be modified as follows,

$$h_i \left(\boldsymbol{x} + \boldsymbol{c}_i \Delta t, t + \Delta t \right) = h_i(\boldsymbol{x}, t) - \boldsymbol{M}_C^{-1} \boldsymbol{S}_C \boldsymbol{M}_C \left[h_i(\boldsymbol{x}, t) - h_i^{\text{eq}}(\boldsymbol{x}, t) \right], \tag{3.50}$$

where $\boldsymbol{M}_C$ is the transformation matrix and $\boldsymbol{S}_C$ is the diagonal relaxation matrix. Both these matrices will be velocity set dependent and, in the case of $\boldsymbol{S}_C$, the relaxation rates for each moment as well, and the values of these will be discussed further on. The concentration macroscopic quantity can be recovered as,

$$C = \sum_i h_i \tag{3.51}$$

Pressure evolution equation

The governing equations for the fluid's behaviour will be given by the continuity and NS momentum equations, Eq.3.52 and Eq.3.53, respectively. These equations are recovered by a Chapman-Enskog analysis of the modified pressure evolution as shown by Fakhari et al. and Tan et al..

$$\frac{\partial p}{\partial t} + \rho c_s^2 \nabla \cdot \boldsymbol{u} = 0, \tag{3.52}$$

$$\rho \left(\frac{\partial \boldsymbol{u}}{\partial t} + \boldsymbol{u} \cdot \nabla \boldsymbol{u} \right) = -\nabla p + \nabla \cdot \left[\mu (\nabla \boldsymbol{u} + \boldsymbol{u} \nabla) \right] + \boldsymbol{F}_b + \boldsymbol{F}_s. \tag{3.53}$$

Here, $\boldsymbol{F}_b$ denotes a body force and $\boldsymbol{F}_s$ a force source term related to the surface tension σ between the gas and liquid, where it is expressed in a continuum from $\boldsymbol{F}_s = \mu_\phi \nabla \phi$. The chemical potential μ_ϕ can then be determined by:

$$\mu_\phi = \frac{48\sigma}{W} \left(\phi - \phi_g \right) \left(\phi - \phi_l \right) \left(\phi - \phi_{\text{avg}} \right) - \frac{3\sigma W}{2} \nabla^2 \phi. \tag{3.54}$$

The term $\nabla^2 \phi$ will be determined using a lattice generalisation that ensures factorizability and isotropy of the scalar in question. The Laplacian for a generic DdQq velocity set will be determined by [51],

$$\nabla^2 \phi = \frac{2}{c_s^2} \left[\sum_{i \neq 0} w_i \phi + (w_0 - 1) \phi \right] \tag{3.55}$$

The distribution function is modified as $f_i^* = f_i c_s^2 + w_i(p - \rho c_s^2)$ and so is the equilibrium distribution function $f_i^{eq,*} = f_i^{eq} c_s^2 + w_i(p - \rho c_s^2)$. The local density ρ will be determined by Eq. 3.56. From now on, the asterisk in the distribution functions will be dropped, but it is important to keep in mind these transformations for the implementation of the current method.

$$\rho = \rho_g + \phi(\rho_l - \rho_g). \tag{3.56}$$

To carry out the collision, Fakhari et al. and Tan et al. utilise an MRT collision operator, which ensures greater stability, allowing for high-density ratios for low Mach numbers. The collision operation will be given by:

$$\hat{f}_i(\boldsymbol{x},t) = \overline{f}_i(\boldsymbol{x},t) - \boldsymbol{M}_p^{-1}\boldsymbol{S}_p\boldsymbol{M}_p\left[\overline{f}_i(\boldsymbol{x},t) - \overline{f}_i^{\text{eq}}(\boldsymbol{x},t)\right] + \Delta t \Gamma_i\left(\boldsymbol{c}_i - \boldsymbol{u}\right) \cdot \boldsymbol{F}_{\text{b}} + $$
$$\Delta t \left[\left(\Gamma_i - \omega_i\right)\left(\rho_l - \rho_g\right)c_s^2 + \Gamma_i\mu_\phi\right]\left(\boldsymbol{c}_i - \boldsymbol{u}\right) \cdot \nabla^M\phi, \tag{3.57}$$

where

$$\Gamma_i = \omega_i\left[1 + \frac{\boldsymbol{c}_i \cdot \boldsymbol{u}}{c_s^2} + \frac{(\boldsymbol{c}_i \cdot \boldsymbol{u})^2}{2c_s^4} - \frac{\boldsymbol{u} \cdot \boldsymbol{u}}{2c_s^2}\right]. \tag{3.58}$$

Fakhari et al. proposed the transformation given by Eq. 3.59 to ensure that the collision scheme remains explicit.

$$\overline{f}_i = f_i + \frac{1}{2}\left(f_i - f_i^{eq}\right) - \frac{\Delta t}{2}\left[\left(\Gamma_i - \omega_i\right)\left(\rho_l - \rho_g\right)c_s^2 + \Gamma_i\mu_\phi\right]\left(\boldsymbol{c}_i - \boldsymbol{u}\right) \cdot \nabla^C\phi - \frac{\Delta t}{2} \tag{3.59}$$

A similar transformation for the equilibrium distribution functions leads to,

$$\overline{f}_i^{eq} = f_i^{eq} - \frac{\Delta t}{2}\left[\left(\Gamma_i - w_i\right)\left(\rho_l - \rho_g\right)c_s^2 + \Gamma_i\mu_\phi\right]\left(\boldsymbol{c}_i - \boldsymbol{u}\right) \cdot \nabla^C\phi - \frac{\Delta t}{2}\Gamma_i\left(\boldsymbol{c}_i - \boldsymbol{u}\right) \cdot \boldsymbol{F}_b \tag{3.60}$$

The streaming is then carried out as,

$$\overline{f}_i(\boldsymbol{x} + \boldsymbol{c}_i\Delta t, t + \Delta t) = \hat{f}_i(\boldsymbol{x},t) \tag{3.61}$$

It is worth noting that $\nabla^M\phi$ and $\nabla^C\phi$ are the gradient operators based on mixed and central finite differences respectively, given by:

$$\nabla^M\phi = \frac{1}{c_s^2\Delta t}\sum_{i\neq0}\omega_i\boldsymbol{c}_i\left[\frac{-\phi\left(\boldsymbol{x} + 2\boldsymbol{c}_i\Delta t, t\right) + 5\phi\left(\boldsymbol{x} + \boldsymbol{c}_i\Delta t, t\right) - 3\phi(\boldsymbol{x},t) - \phi\left(\boldsymbol{x} - \boldsymbol{c}_i\Delta t, t\right)}{4\Delta x}\right],$$
$$\nabla^C\phi = \frac{1}{c_s^2\Delta t}\sum_{i\neq0}\omega_i\boldsymbol{c}_i\left[\frac{\phi\left(\boldsymbol{x} + \boldsymbol{c}_i\Delta t, t\right) - \phi(\boldsymbol{x},t)}{2\Delta x}\right]. \tag{3.62}$$

The zeroth and first moments can be found by employing Eq.3.63, which will determine the pressure and the velocity, respectively.

$$p = \sum\overline{f}_i + \frac{\Delta t}{2}\left(\rho_l - \rho_g\right)c_s^2\boldsymbol{u} \cdot \nabla^C\phi,$$
$$\boldsymbol{u} = \frac{1}{\rho c_s^2}\left[\sum_i\overline{f}_i\boldsymbol{c}_i + \frac{\Delta t}{2}\left(\mu_\phi\nabla^C\phi + \boldsymbol{F}_b\right)\right]. \tag{3.63}$$

Phase-Field validation

The Laplace pressure jump across the interface will be measured to corroborate the implementation of the HZC model discussed in the previous section. The transformation matrix

for the D2Q9 velocity set is given by,

$$
\mathbf{M}_p =
\begin{bmatrix}
1 & 1 & 1 & 1 & 1 & 1 & 1 & 1 & 1 \\
-4 & -1 & -1 & -1 & -1 & 2 & 2 & 2 & 2 \\
4 & -2 & -2 & -2 & -2 & 1 & 1 & 1 & 1 \\
0 & 1 & 0 & -1 & 0 & 1 & -1 & -1 & 1 \\
0 & -2 & 0 & 2 & 0 & 1 & -1 & -1 & 1 \\
0 & 0 & 1 & 0 & -1 & 1 & 1 & -1 & -1 \\
0 & 0 & -2 & 0 & 2 & 1 & 1 & -1 & -1 \\
0 & 1 & -1 & 1 & -1 & 0 & 0 & 0 & 0 \\
0 & 0 & 0 & 0 & 0 & 1 & -1 & 1 & -1
\end{bmatrix}
\tag{3.64}
$$

While the diagonal relaxation matrix is $\mathbf{S} = \mathrm{diag}\,(1,1,1,1,1,1,1,s_\nu,s_\nu)$, where $s_\nu = 1/(\nu/c_s^2 + 0.5)$, the denominator being the relaxation time.

The pressure can be recovered from the distribution function, as shown from 3.63. However, this recovers the whole field. In order to determine the pressure jump across the interface, the pressure inside p_{in} and outside p_{out} are measured as:

$$
\begin{aligned}
p_{\mathrm{in}} &= \left\langle p\,|_{\phi \geqslant 0.999999} \right\rangle \\
p_{\mathrm{out}} &= \left\langle p\,|_{\phi \leqslant 0.000001} \right\rangle
\end{aligned}
\tag{3.65}
$$

Figure 3.2a shows the pressure difference across the interface, showing even better accordance with the theoretical values for different surface tension values. Figure 3.2b shows the relative error of surface tension when the computed pressure difference and respective radius are used to determine the surface tension. Additionally, Figure 3.2b shows that relative error increases for both RK and HZC models with increasing surface tension values. When the radius of the bubble decreases, the relative error also shows an increasing tendency. It is worth noting that even for small bubble radii and considerable surface tensions, the HZC model has a relative error smaller than 10%, significantly smaller than that of the RK model.

A sensitivity analysis was conducted on the width parameter W for a system with a radius $R = 20\,\mathrm{lu}$ and surface tension $\sigma = 0.01\,[\mathrm{mu/tu}^2]$. Table 3.1 shows the results obtained. A width of $W = 4$ was chosen for future simulations to balance sharp interface and accuracy while minimizing spurious velocities.

Table 3.1.: Sensitivity analysis of width W, relative error, and maximum magnitud of the spurious velocities.

W [lu]	δ_σ [%]	U_{max} [lu/tu]
2	1.56	0.00189
3	2.27	0.00039
4	2.53	0.00018

3.4. Model comparison

The presence of (unphysical) spurious currents—mainly close to the bubble interface—is common in all LBM multiphase schemes. To illustrate the phenomenon of spurious currents

(a) Laplace law comparison with the numerical results obtained using the RK and HZC models.

(b) Relative error of the numerical values. An increase in σ implies larger errors for any R as spurious velocities increase.
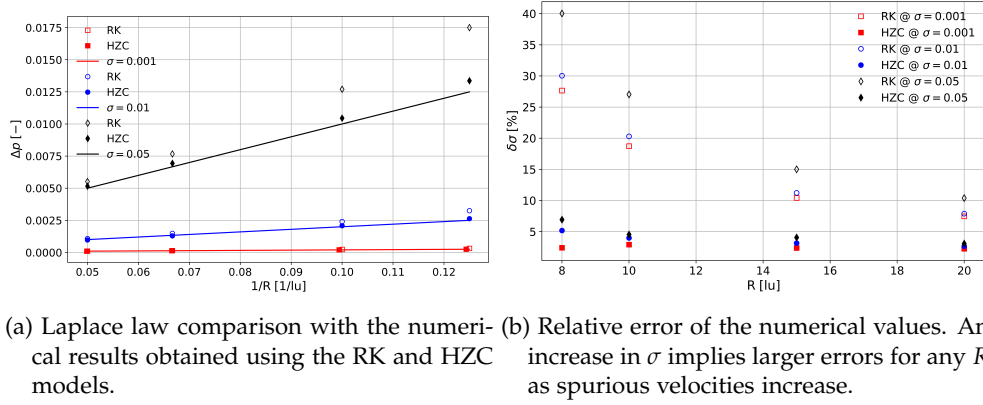
Figure 3.2.: Bubble radius, surface tension and pressure difference relation for a static bubble for the RK (empty characters) and the HZC (filled characters) models.

and show that the HZC and RK models have smaller spurious currents than the SC model, the velocity field is shown in Figure 3.3. The input parameters used are reported in Table 3.2 Note that the areas with the most significant spurious currents are closer to the bubble interface in the RK simulation than in the SC and HZC simulations, as these latter two are diffuse methods. Furthermore, we see that the maximum spurious current in the RK and HZC simulations is an order of magnitude smaller than those present in the SC results. The spurious velocities are the smallest in the HZC method, attributed mainly to the interface potential force form and the stable discretization, which estimate various derivatives [34, 48]. On the other hand, implementing this model is quite complex and computationally expensive, requiring around two times more CPU computation per time-step than the RK model for a stationary bubble case with density ratios of $O(10^2)$ [52]. It is computationally expensive as the numerical implementation involves the discretization of many directional derivatives, which need to be evaluated in every lattice direction.

Table 3.2.: Input parameters for the static bubble simulations for the RK, HZC, and SC cases. For the RK $\rho_l = \rho_A$ and $\rho_g = \rho_B$.

Method	ρ_l	ρ_g	τ_l	τ_g	σ	G	β	α_B	M
RK	1.0	0.10	1.0	1.0	0.01	-	0.7	0.2	-
HZC	1.0	0.10	1.0	1.0	0.01	-	-	-	0.167
SC	1.72	0.15	1.0	1.0	-	-4.8	-	-	-

To simulate bubble growth in AWE the multiphase method should handle density ratios of $O(10^2)$. The implemented SC method, therefore, is not an option as it would not comply with this requirement. Both RK and HZC methods can handle large density ratios. While the RK method is computationally less taxing than the HZC, its superior velocities are slightly higher. The HZC model, by having smaller spurious velocities, the mass transport around the liquid-gas interface will be less affected by unphysical convection. The HZC method is preferred over the SC and RK methods to develop an LBM method for AWE that can track bubble growth. In Appendix A, a qualitative comparison of the three methods and the Free Energy method can be found.
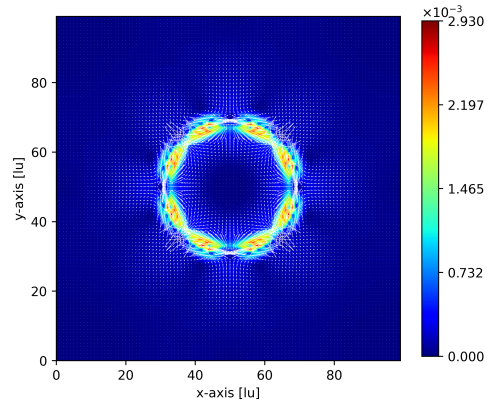
(a) Velocity contour for the SC model.
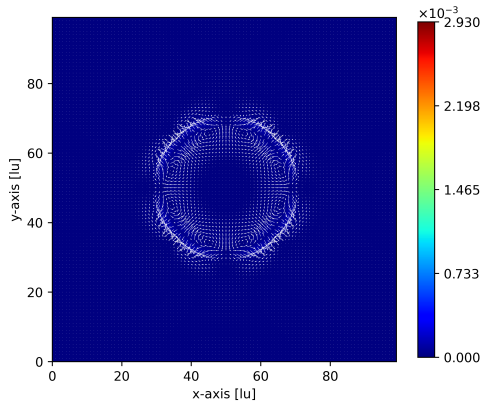
(b) Velocity contour for the RK model.
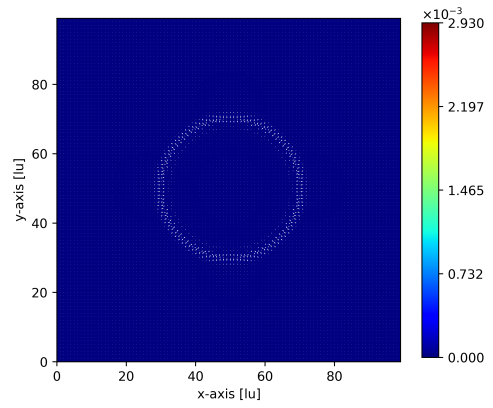
(c) Velocity contour for the HZC model.

Figure 3.3.: Velocity contour comparison after simulations convergence.

4. Bubble Growth in a Supersaturated Domain

Bubble dynamics, particularly bubble growth, are deeply intertwined with the transport mechanisms described in the following chapter. The growth or shrinkage of a bubble attached to an electrode provides valuable insights into the chemical potential in its vicinity. If the dissolved H_2 concentration exceeds the supersaturation level, the bubble will grow; conversely, if the surrounding electrolyte is undersaturated, the bubble will shrink [53]. While not conventional, the system in the present work will be considered as SCMP. H_2 will be considered as the only component in the bulk liquid, which will transfer into the gaseous phase. This can be justified as locally near the bubble, H_2 will be highly supersaturated. Having a single component H_2 system serves as a simplification to avoid coupling other electrochemical LB solvers such as the Nernst-Planck (for mass transport) and Poisson solvers (for electric field).

This chapter presents a brief discussion of the different bubble growth regimes, followed by a grid sensitivity study. The modified HZC model, as presented previously, is implemented, and the mass transfer across the interface is then validated using Newman analytical solution for a spherical bubble in pure diffusive regimes. Bubble growth is then analysed under supersaturated conditions.

4.1. Bubble growth regimes

There are three recognised growth regimes for bubble evolution in AWE. Each stage of growth can be described by:

$$R(t) = \beta t^x. \tag{4.1}$$

Here, $R(t)$ represents the time-dependent radius of the bubble, t is the time, β is a growth coefficient primarily dependent on the current density, and x is the time exponent that determines the growth rate [26]. The first growth stage is hydrodynamically controlled and lasts up to $t = 10$ms. This process is governed by the inertia of the liquid surrounding the bubble and can be described by the Rayleigh equation:

$$R(t) = \left(\frac{2\Delta P}{3\rho_{\text{ele}}}\right)^{0.5} t. \tag{4.2}$$

In this equation, ρ_{ele} is the density of the electrolyte. During this period, bubble growth is driven by high internal excess pressure, which is related to the surface tension of the liquid-vapor interface.

The second stage is governed by diffusion-controlled growth, occurring when the liquid surrounding the bubble becomes saturated, facilitating the diffusion of dissolved gas from

the bulk electrolyte towards the bubble. This stage takes place from $10\text{ms} < t < 100$ ms and is described by:

$$R(t) = C\,(\text{D}t)^{1/2}\,,\tag{4.3}$$

where D is the diffusion coefficient, and C is an experimentally determined coefficient.

In the third stage, bubble growth is limited by the electrochemical reaction rate, and the growth can be represented as:

$$R(t) = \beta t^{1/3}\tag{4.4}$$

In this case, the time exponent $x = 1/3$ reflects the constant rate of gas addition to the bubble. This final mode of growth becomes dominant as the bubble-to-electrode diameter ratio increases. Deviations from reaction or diffusion-governed growth are observed when an underdeveloped dissolved gas boundary layer is present.

4.2. Physical to LB quantities

Adequate conversion factors are essential to map the physical properties of the system in question to the lattice units and back again to physical units for postprocessing. Three fundamental dimensions are sufficient to generate the dimension of any mechanical quantity; thus, three independent conversion factors are required to define a unique non-dimensionalisation framework. For the present study, the three quantities used will be length, time, and mass. To create a link between physical variables and simulation variables, the parameters previously mentioned will be non-dimensionalised as:

$$\Delta t^* = \frac{\Delta t}{C_t},$$
$$\Delta x^* = \frac{\Delta x}{C_x},$$
$$\rho^* = \frac{\rho}{C_\rho}.$$

The non-dimensionalised variables have a subscript *, and C denotes the conversion factors. In lattice units, the values $\Delta x^* = 1$ lu, $\Delta t^* = 1$ tu, and $\rho_l^* = 1$ mu are assigned. Table 4.1 shows the physical and lattice values of the parameters used for all simulations in the present study.

4.3. Grid independency study

In LB simulations, as in other standard CFD methods, the computational domain that discretises the physical domain can affect the numerical results. A grid independence study must be performed to determine the optimal number of lattice nodes required for simulation. As in most LB simulations, the spatial discretisation is equal to unity (i.e., $\Delta x^* = 1\text{lu}$), so the node resolution will depend on a reference scale, which will be case-dependent. However,

Table 4.1.: Relevant physical variables for AWE at 80°C and 5 bar [25]. Unless specified otherwise, all the parameters remain constant for all the simulations.

Parameters	Lattice value	[Lattice unit]	Physical value	[SI unit]
Δx	1.0	[lu]	1.0×10^{-6}	[m]
Δt	1.0	[tu]	4.5×10^{-9}	[s]
ρ_l	1258	$\left[\text{mu/lu}^3\right]$	1258	$\left[\text{kg/m}^3\right]$
ρ_g	1.0	$\left[\text{mu/lu}^3\right]$	1.0	$\left[\text{kg/m}^3\right]$
ν_l	3.02×10^{-3}	$\left[\text{lu}^2/\text{tu}\right]$	6.7×10^{-7}	$\left[\text{m}^2/s\right]$
ν_g	1.46×10^{-1}	$\left[\text{lu}^2/\text{tu}\right]$	3.24×10^{-5}	$\left[\text{m}^2/s\right]$
D_l	2.61×10^{-5}	$\left[\text{lu}^2/\text{tu}\right]$	5.8×10^{-9}	$\left[\text{m}^2/s\right]$
D_g	1.15×10^{-1}	$\left[\text{lu}^2/\text{tu}\right]$	2.56×10^{-5}	$\left[\text{m}^2/s\right]$
$C_{H_2,l}$	100	$\left[\text{mu/lu}^3\right]$	49603	$\left[\text{mol/m}^3\right]$
$C_{H_2,g}$	3.24×10^{-4}	$\left[\text{mu/lu}^3\right]$	0.16	$\left[\text{mol/m}^3\right]$
σ	0.891	$\left[\text{mu/tu}^2\right]$	0.044	[N/m]

for most simulations in the present study, the bubble radius will be $R = 20\ \mu$m unless specified otherwise. The present work will use a D2Q9 velocity set to carry out all 2D simulations. Figure 4.1 shows the computational domain, illustrating the dependence of the domain size on the bubble radius. The domain sizes are $L_x = L_y = 5R$ to ensure bubble growth without the bubble interacting with itself, as periodic boundary conditions are imposed for the three distribution functions: pressure, phase field and concentration. Three resolutions are used which can be seen in Table 4.2. A final simulation time of $t = 0.000225$ s an arbitrarily chosen time, which is long enough to see the systems resolution dependence.

Table 4.2.: Grid resolution and their respective spatial, temporal, radial and simulation runtime values.

Resolution	$\Delta x\ [\mu m]$	$\Delta t\ [ns]$	$R\ [lu]$	Runtime
1X	1.0	4.5	20	30 min
2X	0.5	1.125	40	4 hours
3X	0.333	0.5	60	2.5 days

Figure 4.2 illustrates the bubble radius growth for each grid resolution. The radius of the bubble is determined as the average value of the distance between the center of the bubble and the interface (given by the condition $\phi = 0.5$). As expected, increasing the grid resolution results in a more refined representation of the bubble interface, leading to smoother mass transport from the liquid to the gaseous phase. The maximum bubble radius varies between grids, with a difference of 0.1377 μm between the 1X and 2X grids and 0.0924 μm between the 2X and 3X grids. The decrease in the difference between the 2X and 3X grids compared to that of the 1X and 2X grids shows that the domain becomes more resolved as the spatial and temporal discretisations increase, as expected.

Since the current implementation is realised in Python and uses a single CPU core to run the simulations, extending the current method to open-source GPU/multicore-enabled codes such as LBPM[1] is essential to obtain the best results. Thus, for the current study, the 1X grid
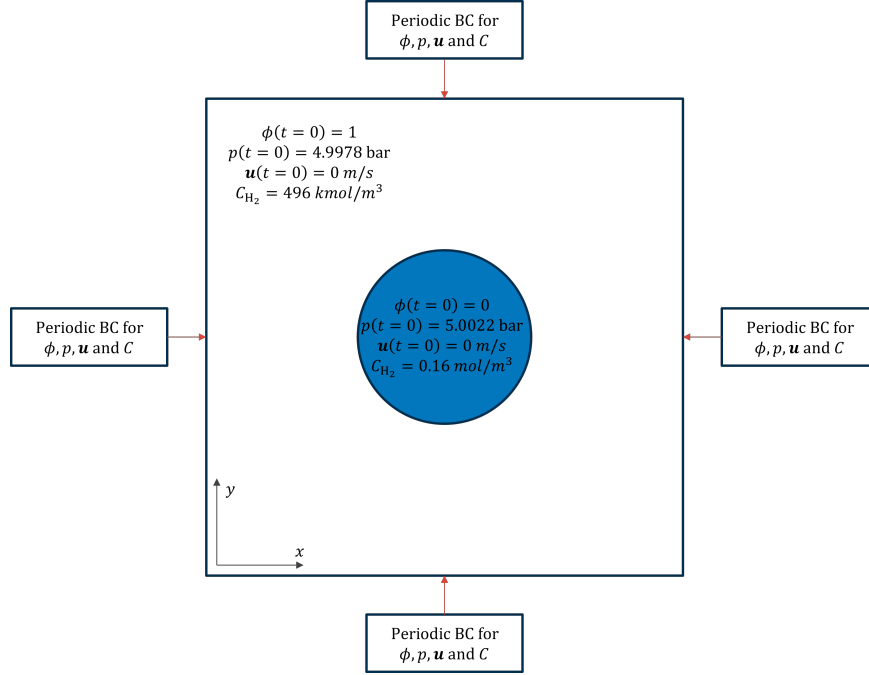
Figure 4.1.: Boundary and initial conditions for the super saturated domain simulations.

resolution was used for most of the simulations. The aim of this grid dependency study was to highlight the existence of grid-resolution dependency of the results when using the 1X grid due to the limitations in computational power. The 1X grid was chosen to be able to run simulations for longer, in order to reach longer physical times as the computational demand would be much lower.

It is worth noting that the value of $C_{H_2, 1}$ is very large, which was required to ensure bubble growth for shorter physical times given the computational cost of the current LB model.

4.4. Validation

4.4.1. Mass transfer across the interface

The mass transfer within a bubble is validated under a purely diffusive regime, where the bulk electrolyte remains a stagnant fluid, i.e., $\boldsymbol{u}_l = 0$. Newman [54] proposed an analytical solution for the normalised concentration inside a gas bubble, by deriving a solution for mass transfer controlled by pure diffusion within a sphere. The time evolution of the Sherwood number Sh, can be determined for a fixed concentration at the surface and a uniform initial concentration within the sphere. The instantaneous radial profile of the normalised

---

[1]More information about the parallelised/GPU enable open source code Lattice Boltzmann Methods for Porous Media (LBPM) can be found at https://lbpm-sim.org/
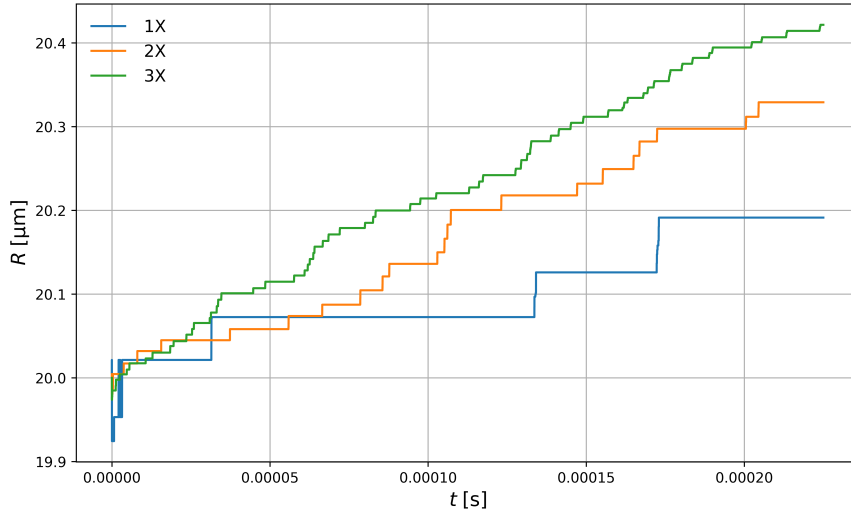
Figure 4.2.: Radius growth of a bubble in a supersaturated domain for different grid resolutions.

concentration is given by:

$$
c'(r', t') = \begin{cases}
1 + \dfrac{2}{r'} \displaystyle\sum_{n=1}^{\infty} \dfrac{(-1)^n}{n\pi} \exp\left(-[n\pi]^2 t'\right) \sin(n\pi r'), & \text{for } r' > 0, \\[3mm]
1 + 2 \displaystyle\sum_{n=1}^{\infty} (-1)^n \exp\left(-[n\pi]^2 t'\right), & \text{for } r' = 0.
\end{cases}
\tag{4.5}
$$

The corresponding instantaneous Sherwood number is expressed as:

$$
Sh\left(t'\right) = \frac{2\pi^2}{3} \frac{\sum_{n=1}^{+\infty} \exp\left(-[n\pi]^2 t'\right)}{\sum_{n=1}^{+\infty} \frac{1}{n^2} \exp\left(-[n\pi]^2 t'\right)}
\tag{4.6}
$$

Figure 4.3 shows the instantaneous Sh plotted against the dimensionless time t'. The data used to set up the simulation is listed in Table 4.3.

Table 4.3.: Input parameters used to validate Eq. 4.6. The chosen parameters are based on those used by Zheng et al..

ρ_l/ρ_g	ν_l/ν_g	D_l/D_g	C_l/C_g	He	σ	M	W	R
10.0	1.0	0.05	5.0	0.2	0.005	0.167	4.0	60.0

Numerically, the Sherwood number can be determined by:

$$
Sh(t') = \frac{k_l D_b}{D_l},
\tag{4.7}
$$

where $D_b = 2R_b$ is the diameter of the bubble, and k_l is the average mass transfer coefficient. The mass variation of the bubble between two consecutive time steps is calculated as follows
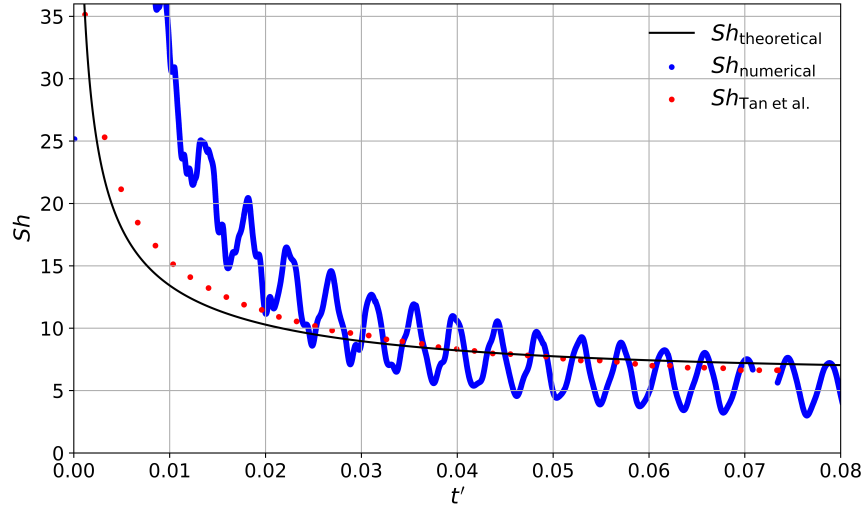
Figure 4.3.: Instantaneous Sherwood number versus t'. The blue dots are the results obtained using the HZC model implemented in this study, the red dots are data from Zheng et al. [1], and the black line is Eq. 4.6.

[1, 55]:

$$k_l = \frac{\sum_n C_{t+1} V_{t+1} - \sum_n C_t V_t}{S_b \Delta t \Delta C},$$

(4.8)

where C_{t+1} is the gas concentration in the volume V_{t+1} at time step $t + 1$, S_b is the bubble surface area for mass transfer, and ΔC is the concentration difference between the interface concentration $\overline{C}_{int}$, and the gas phase concentration, $\overline{C}_g$. The average concentration of the interface and the gas phase is determined using $\phi = 0.5$ and $\phi < 0.5$, respectively.

The results obtained oscillate around the analytical value since the relaxation times for both fluids for the hydrodynamic equation make the system over-relaxed (i.e., $\tau_{\nu,l} = \tau_{\nu,g} = 0.85$). The relaxation time for the concentration distribution for the liquid, also enforce the system to be over-relaxed as $\tau_{C_l} = 0.53$. The simulation exhibits substantial oscillations at the beginning; however, for larger values of t', the amplitude decreases compared to the initial amplitude. The discrepancy in the results is attributed to the discretisation of the Laplacian operator in Eq.3.54. Neither Zheng et al. nor Fakhari et al. specify how this Laplacian operator is discretised, hence the choice of 3.55 may differ from what they actually used. The initial value of Sh differ as the Laplacian operator is highly sensitive to large values of the phase field gradient at the beginning of the simulation. However, for $t' > 0.02$, the numerical results oscillate about the analytical result.

The results obtained by Zheng et al. follow a similar trend, where for $t' < 0.04$, the Sh is overpredicted, and for $t' > 0.05$, it is underpredicted. It is worth noting that Zheng et al. do not specify how they sampled the data, potentially aligning the data to the analytical solution to show better agreement. These results validate that the implementation of the HZC model is correct. An MRT collision operator for the concentration distribution function was also implemented, however for this comparison it was not included, to validate the data using the same relaxation scheme.

4.4.2. Bubble growth

To validate the diffusive growth regime explored in the section 4.1, a single 5.045μm bubble is placed in a supersaturated domain far away from the cathode. The spatial and temporal resolutions are $\Delta x = 0.0901\mu$m and $\Delta t = 1.001$ns, respectively. The present simulation will correspond to a 2.8X resolution. The lattice bubble size radius is set to 56lu with a domain size of $L_x = L_y = 280$lu. Furthermore, the solubility and concentration far from the bubble are assumed constant. Figure 4.1 shows the boundary and initial conditions of the system.

The growth of the bubble is shown over time in Figure 4.4 with a power law fit representing a diffusion-controlled growth of $R \sim t^{0.5}$ [26, 56]. The predicted radius and the power law coincide, showing that implementing the current LB method to track mass transfer across a multiphase interface is adequate.
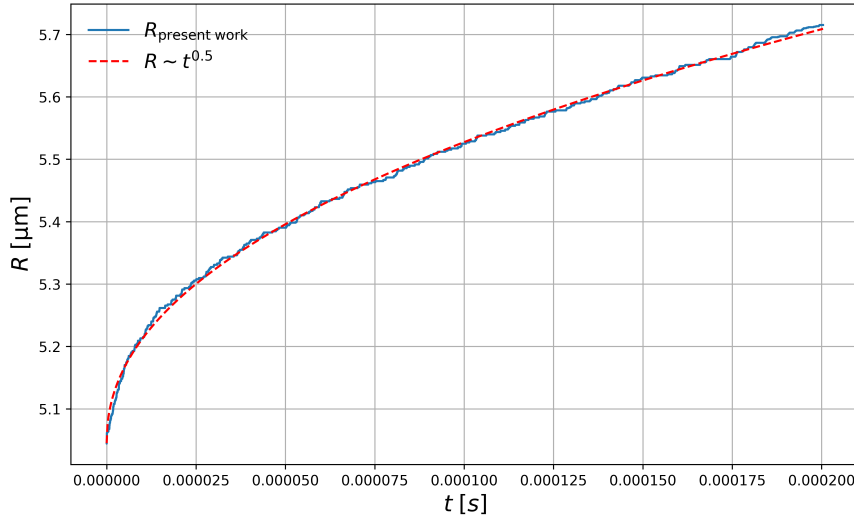

Figure 4.4.: Bubble growth in a supersaturated domain. The blue line shows the simulated data, while the red line shows a fit corresponding to a power law type $R \sim t^{0.5}$.

The concentration field of the bubble at $t = 0.2$ ms is shown in Figure 4.5 with the initial size of the bubble denoted by the black line. The concentration field shows some darker spots that arise due to instabilities present because of the large differences in magnitudes of the physical parameters of liquid and gas, mainly D_l and D_g. The spatial and temporal resolutions ensure that all four relaxation times are as close to or larger than 0.51. The downside of such small Δx and Δt is that this increases the conversion factor for surface tension, which causes instabilities due to the increase in unphysical spurious velocities at the interface.

Concentration and pressure evolution

The pressure inside the bubble must be analysed to ensure a correct pressure and concentration coupling via the phase field source term (last term on the right of Eq.3.35). The bubble
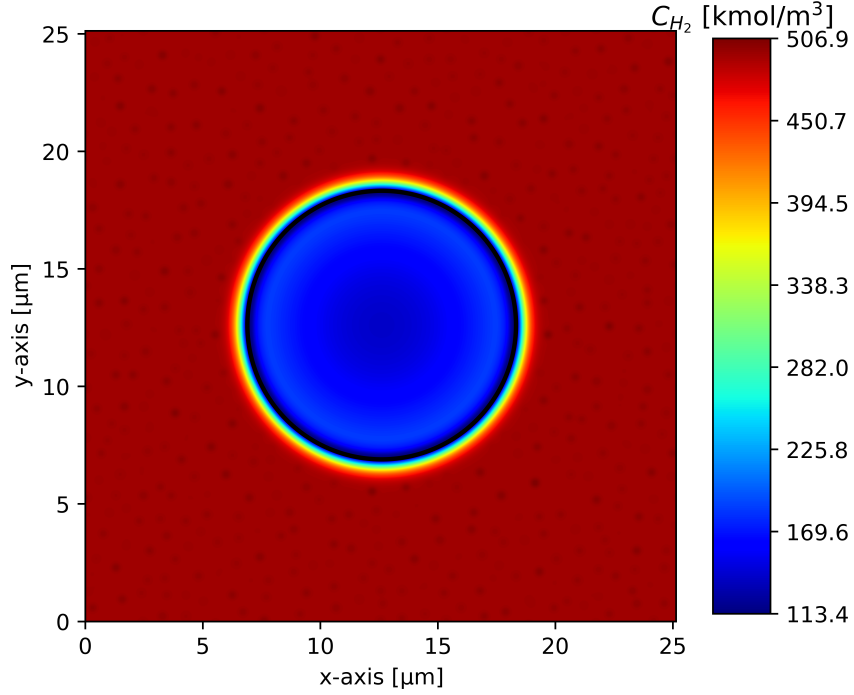
Figure 4.5.: C_{H_2} contour at t = 0.2 ms. Instabilities arise after 0.2 ms as the surface tension generates significant unphysical spurious currents that in the liquid domain.

radius, spatial, and temporal resolutions are changed to those shown in Table 4.1 to: i) ensure the stability of the simulation because smaller δx and δt lead to large surface tension but also large spurious velocities, ii) allow the simulation to run for longer physical time by reducing the computational cost.

One of the main assumptions of Zheng et al. for coupling the Phase-field method to the concentration evolution is that the gas-liquid interface follows Henry's Law. Inside the bubble, the gas will behave like an ideal gas; the pressure will be,

$$p_{\overline{C}_{H_2}} = \overline{C}_{H_2} R_u T, \tag{4.9}$$

where $\overline{C}_{H_2}$ is the concentration of the gas in mol/m^3, T the temperature in K and R_u is the universal gas constant. The average value of concentration in the gas is taken as,

$$\overline{C}_{H_2} = \left\langle C_{H_2} \mid_{\phi \leqslant 0.000001} \right\rangle \tag{4.10}$$

The pressure can also be determined using the zeroth order moment of the pressure distribution function, as shown by Eq. 3.63, we denote it as p_R. Table 4.4 shows the pressure, determined via both methods, at different time steps. The values of pressure deviate from the initial condition of 5 bar, since the solution has not reached equilibrium. However, the values obtained using the ideal gas law and the zeroth order moment produce similar results. The highest deviation is at $t = 20$ ms, where the value obtained via the pressure distribution and the ideal gas law are 1.609 and 1.198, respectively. It is worth noting that pressure values have an increasing tendency for both methods. The simulation should have

been run for longer physical times to determine whether the system reached an equilibrium pressure of 5 bar- the initial condition specified.

Table 4.4.: Input parameters used to validate Eq. 4.6. The chosen parameters are those used by Zheng et al..

Time [ms]	$R\,[\mu m]$	$\overline{C}_{H_2}\,[kmol/m^3]$	$p_R\,[bar]$	$p_{\overline{C}_{H_2}}\,[bar]$
0	20.00	0.110	0.049	0.053
1	20.76	155.056	0.380	0.455
2	21.35	312.746	0.678	0.918
4	22.51	548.173	1.198	1.609

Concentration profiles

The interface of the gas-liquid system is analysed using the two-resistance model proposed by Lewis and Whitman [57]. Lewis and Whitman state that diffusion rates control the species transfer through each phase. Additionally, the diffusion rate through the gas-liquid interface will be instantaneous, thus maintaining equilibrium at all times, thanks to Henry's Law. Figure 4.6 shows how a supersaturated liquid with H_2 will guide the mass transport. At the interface, there will be no resistance to transport, the two concentrations will remain in equilibrium, and their values can be related by Henry's law [58],

$$He = \frac{C_{l,H_2}}{C_{g,H_2}}.$$ (4.11)

The H_2 concentration profile is shown in Figure 4.7 at different times. After $t > 0$ms,
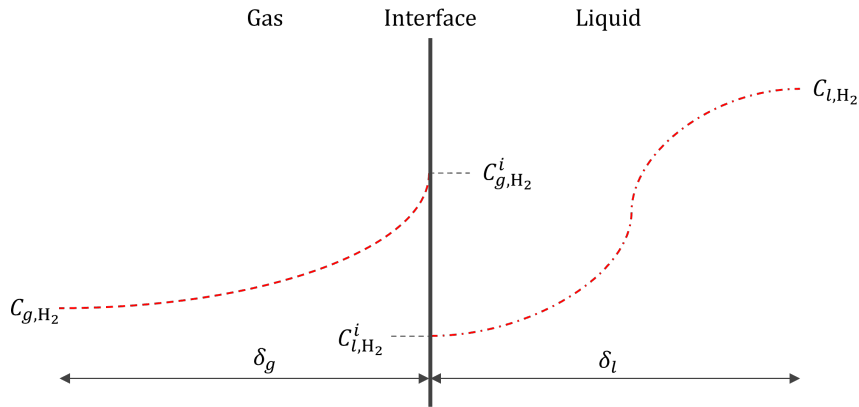
Figure 4.6.: Theoretical concentration profile around the interface, where δ_g and δ_l are the interfacial film thickness of the gas and liquid, respectively.

the interface dynamics develop as the concentration starts to follow Henry's Law. At $t = 1, 2$ and 4 ms, the jump at the interfaces has values of 2.09, 2.95 and 4.58, respectively. These values do not correspond to the specified $He = 310$ for H_2 at 5 bar and $80°C$. However, they do show an increasing tendency, which implies that the system has not reached equilibrium.

Figure 4.7.: Concentration profile at different time steps for a H_2 bubble in a supersaturated domain. The inset represents the cross section at which the conc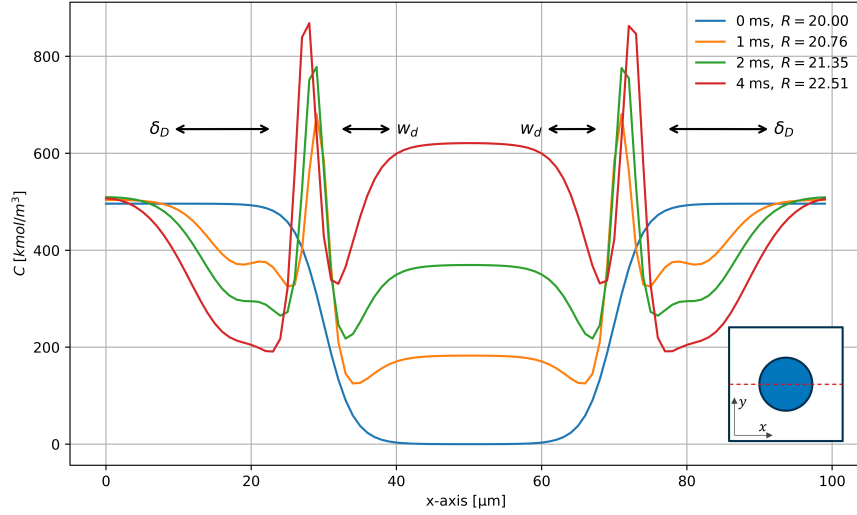entration is being sampled. δ_D is the diffusive boundary layer of the bubble and w_d is the width of the dip shown inside the bubble.

The concentration dip, observed inside the bubble corresponds to the numerical reaction of a sharp increase at the interface. The dip width w_d decreases as at $t = 1$ ms, the number of voxels following a convex curve is six; meanwhile, at $t = 4$ ms, only four.

Diffusive boundary layer

The diffusive boundary layer thickness δ_D, in Figure 4.7, is shown on the outer regions of the plotted curves. The boundary layer thickness around the bubble is defined by,

$$\delta_D(t) = \frac{\left\langle C_{H_2}\big|_{\phi=0.5} - C_{H_2,0}\big|_{\phi=0.5}\right\rangle}{\left\langle \partial C_{H_2}/\partial x\big|_{\phi=0.5}\right\rangle},\tag{4.12}$$

where $C_{H_2,0}$ is the initial concentration profile. This relation is plotted against time in Figure 4.8, which shows a constant slope for $t < 0.004s$. This indicates that the system has not reached equilibrium as the gradient of δ_D is only starting to decrease for $t > 0.004s$ [25, 59]. When the system reaches equilibrium, δ_D should approximate a constant value given that the system does not have any H_2 sources.

4.5. Three Dimensional Bubble Growth

To extend the work of Zheng et al., a three-dimensional model is developed using two different velocity sets: D3Q7 and D3Q19. For ADEs, lower-order isotropic lattices such as D2Q5 and D3Q7 are sufficient as ADE only requires the zeroth and first moments to be recovered [31]. However, Memon [60] found that a D3Q7 velocity set has too few stencils
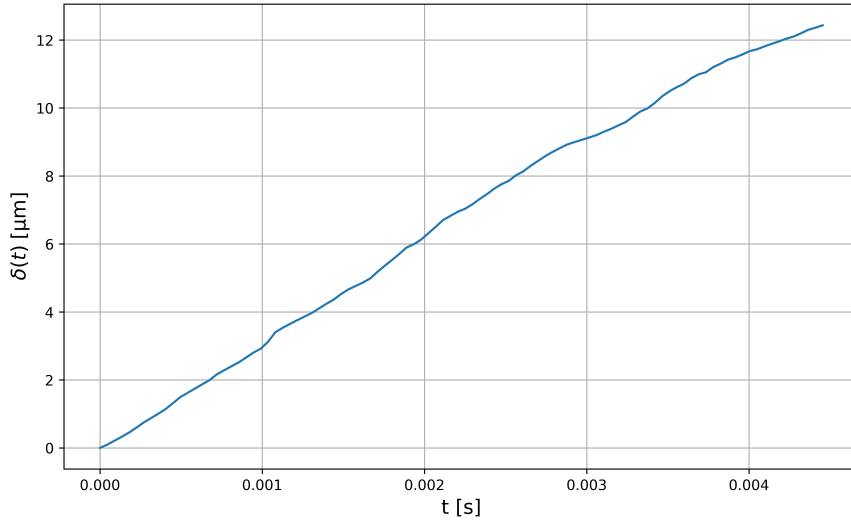
Figure 4.8.: Concentration boundary layer thickness δ_D in a supersaturated domain.

to be isotropic; the leading error term will only be second-order accurate when calculating the Laplacian of a scalar. Higher-order velocity sets, such as D3Q19, which offer up to fourth-order accuracy for the leading term, are preferred for determining the Laplacian of a scalar.

The pitfall of using D3Q19 for all distribution functions in the present model is the increase of 24 more velocity set computations per time step, which drastically hampers the simulation runtime. Nevertheless, to test whether using a D3Q7 velocity set is possible for the concentration and phase field, a 3D method is developed such that either velocity set, D3Q7 and D3Q19, can be chosen to be used for the aforementioned distributions. To ensure symmetry, the third dimension will also be equal in length to the others, i.e. $L_x = L_y = L_z = 100$ lu.

Figure 4.9 shows the phase field for the D3Q19 and D3Q7 velocity sets. At a physical time of $t = 10\mu s$ the D3Q7 case shows a lack of isotropy in the diagonal directions, a phenomenon not evidenced in the D3Q19 case. The velocity magnitude contours, shown in Figure 4.10 for all three different planes corroborates the previous observations, as high velocity magnitudes are seen along the stencil directions for the D3Q7 case. On the other hand, the D3Q19 case shows lower velocity magnitude and radial symmetry as there is a region of high velocity around the bubble interface.

The D3Q19 method implementation also shows bubble growth, as shown in Figure 4.11, albeit the physical time simulated is short. Simulating for extended periods was impossible as the single core implementation took 1.5 days to run only $20\mu s$. Therefore, no further development was realised in the 3D implementation in the present investigation.

Figure 4.9.: Thee dimensional ϕ at different times. The three images on the left columns use a D3Q19 stencil for all distribution functions, while the right column images use a D3Q7 stencil for the concentration and phase fields. Non-isotropic behaviour is observed for the D3Q7 case.
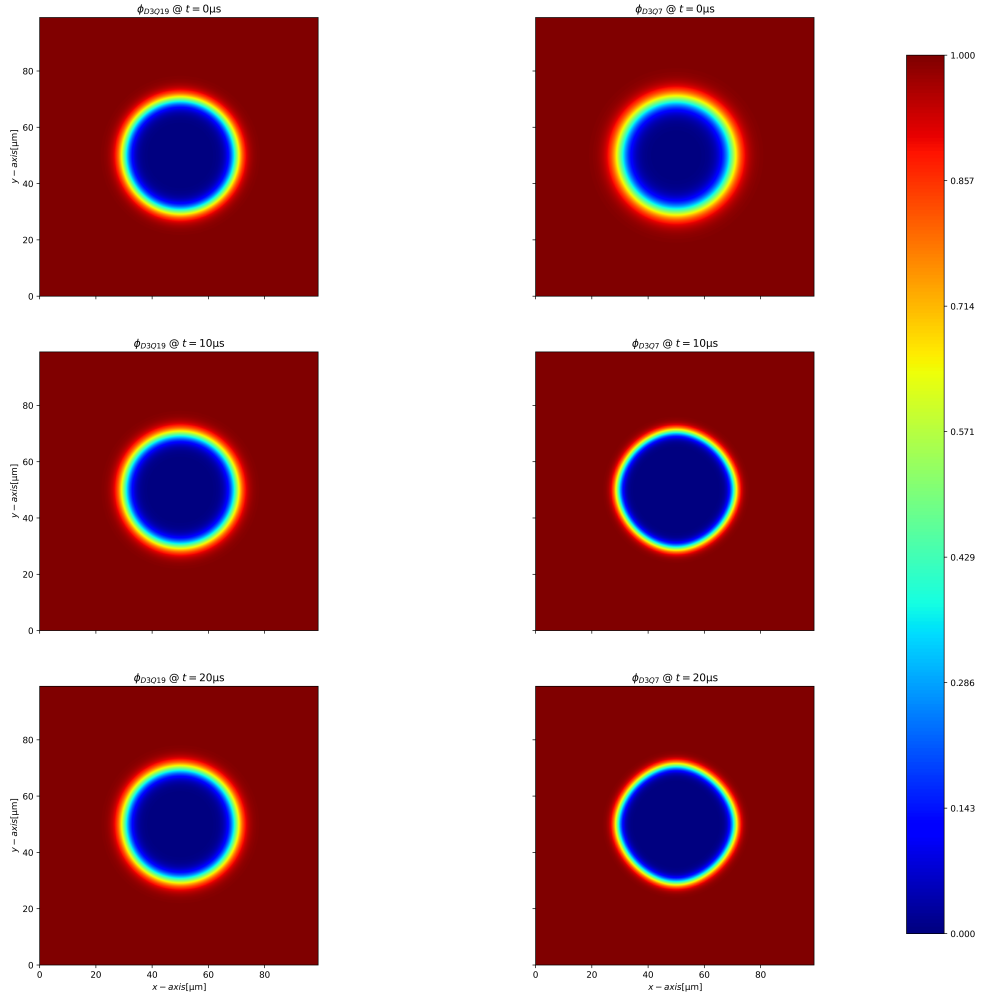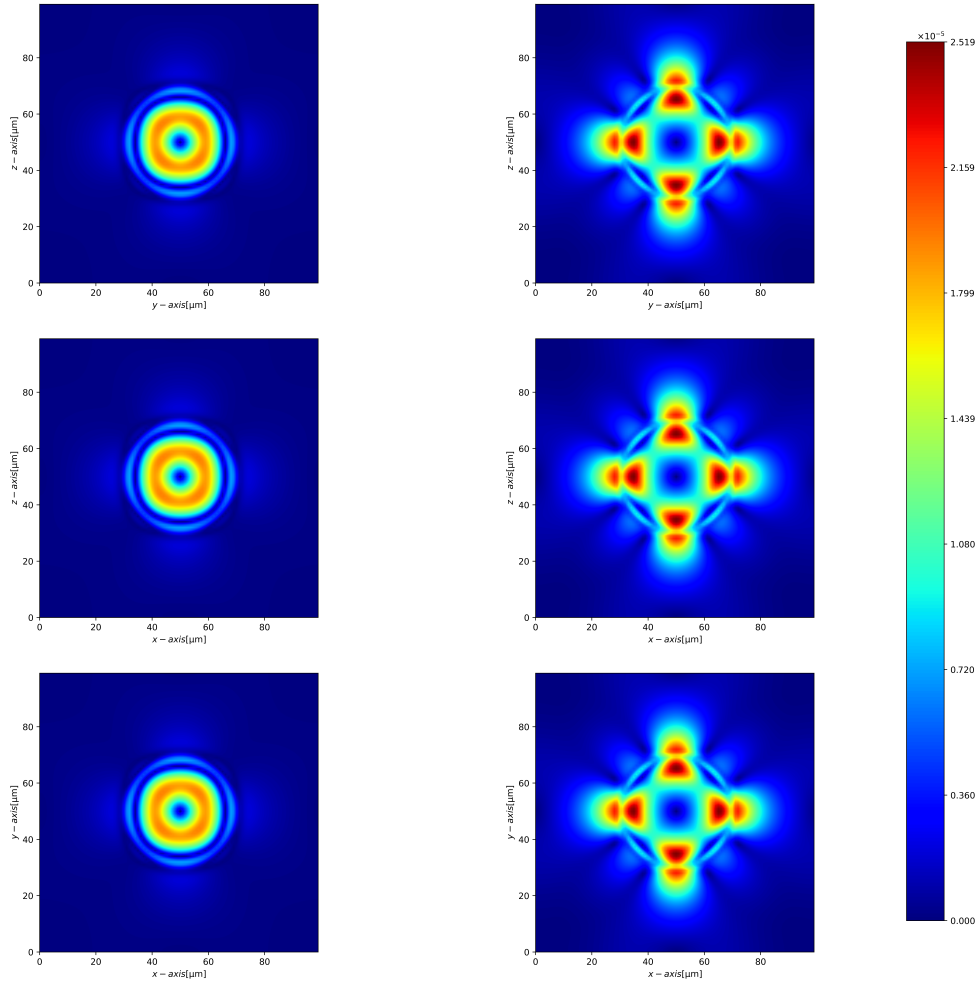
Figure 4.10.: Thee dimensional U at different times. The three images on the left columns use a D3Q19 stencil for all distribution functions, while the right column images use a D3Q7 stencil for the concentration and phase fields. Higher velocity magnitude is observed for the lower stencil velocity set
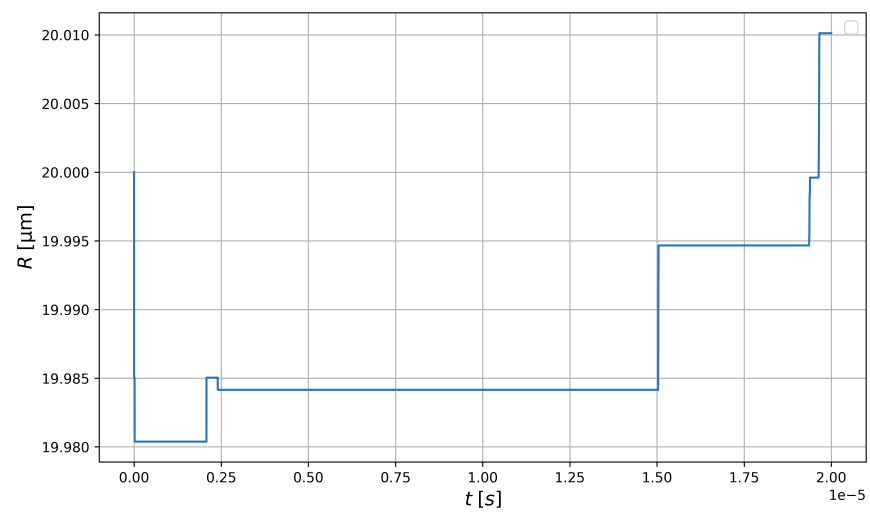
Figure 4.11.: Three-dimensional bubble growth in a supersaturated domain.

5. Bubble Growth near an electrode

In the previous chapters, while the dynamics of H_2 bubbles in AWE were analysed, the presence of the cathode and electrochemical reactions and their consequences on bubble growth were omitted. Electrochemical reactions are the heart of the operation of any electrochemical device. The main idea behind these reactions is the movement of ions due to diffusion, convection and migration, while oxidation and reduction reactions facilitate the production of these ions. The potential difference between the electrodes and the electrolytic solution influences the interplay of reactions and ion transfer. The mass transport phenomena, the thermodynamics of the systems, and the reaction kinetics also affect the latter. A brief description of the driving force of electrochemical reactions and some relevant electrolyte-electrode physics is explored in Appendix B.

The present chapter will explain the mass transport mechanism in AWE, followed by the implementation of a constant H_2 boundary condition. The latter part of the chapter will focus on the results of implementing the constant flux boundary condition.

5.1. Transport mechanism

The transport of ions in an electrolyte is governed by three primary factors: electric fields (migration), concentration gradients (diffusion), and fluid motion (convection). All these mechanisms play significant roles in determining the net flux of ions in the present study [13, 61]. Hence, the collective effects of migration, diffusion, and convection are vital considerations.

5.1.1. Migration

Migration is driven by an electric field induced by gradients in electric potential. This field prompts cations to move against the potential gradient and anions to move with the potential gradient. The velocity of ions in response to this electric field is termed the migration velocity ($\boldsymbol{u}_{i,M}$), as defined by:

$$\boldsymbol{u}_{i,M} = -z_i \nu_i F \nabla \Phi, \tag{5.1}$$

where ν_i is the mobility which is a proportionality factor that relates how fast an ion moves in response to an electric field. It has units of $cm^2 mol/Js$. The migration velocity and the concentration of each species determine the flux density using the Nernst-Einstein equation, which relates the diffusion coefficient D_i and the ionic mobility of a species,

$$D_i = RT\nu_i. \tag{5.2}$$

The migration flux is therefore given by,

$$\boldsymbol{N}_{i,M} = C_i \boldsymbol{u}_{i,M} = -\frac{C_i z_i D_i F \nabla \Phi}{RT}. \tag{5.3}$$

5.1.2. Diffusion

For any multicomponent system, concentration gradients will exist, which induces mass transport through diffusion (Fick's equation for a dilute solution), as described by the flux density equation:

$$\boldsymbol{N}_{i,D} = -D_i \nabla C_i. \tag{5.4}$$

5.1.3. Convection

Bulk fluid movement can occur through natural or forced convection. Natural convection arises from density gradients, while forced convection results from mechanical stirring or pressure gradients. The species flux density due to convection ($\boldsymbol{N}_{i,C}$) is given by:

$$\boldsymbol{N}_{i,C} = C_i \boldsymbol{u}_b, \tag{5.5}$$

where $\boldsymbol{u}_b$ is the bulk velocity. While bulk convection alone cannot generate a net current in an electrically neutral solution, it aids in solution mixing and facilitates reactant transport toward and products away from the electrode interface.

The overall flux density considering all three transport mechanisms is given by Eq. 5.6, which is also commonly known as the Nernst-Planck equation.

$$\boldsymbol{N}_i = -\frac{C_i z_i D_i F \nabla \Phi}{RT} - D_i \nabla C_i + C_i \boldsymbol{u}_b. \tag{5.6}$$

5.2. Constant hydrogen flux at an electrode

The domain will remain the same, albeit the boundary conditions are modified. The new boundary conditions will be implemented using a wet node approach, which assigns suitable values for the unknown boundary populations such that the known and constructed populations reproduce the intended physics at the boundary. Figure 5.1 shows a diagram of a wet node approach at the cathode. The equilibrium scheme is used to determine the unknown populations. The equilibrium scheme is possibly the simplest way to specify LB boundary conditions. It enforces the equilibrium distribution on the post-streaming boundary populations, where the equilibrium distribution populations are determined using the macroscopic quantities at the boundary as [62],

$$
\begin{aligned}
f_i(\boldsymbol{x}_b, t) &= f_i^{\text{eq}}(p_w, \boldsymbol{u}_w), \\
g_i(\boldsymbol{x}_b, t) &= g_i^{\text{eq}}(\phi_w, \boldsymbol{u}_w).
\end{aligned}
\tag{5.7}
$$

For the $h_i(\boldsymbol{x}_b, t)$, the unknown populations will be determined differently, as will be explained in a later section.
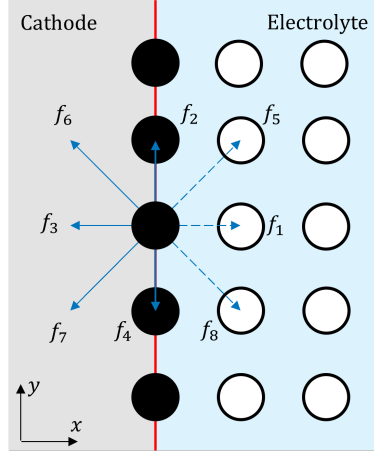
Figure 5.1.: Left boundary coinciding with vertical lattice links. The known boundary populations are represented by continuous vectors the unknown populations by dashed vectors

Pressure and phase no-slip boundary condition

The boundaries for the different distribution functions are modified in the following section. The top and bottom sides of the domain will remain as periodic boundaries for all the distribution functions. The left boundary is the cathode, where a no-slip boundary condition is imposed for the pressure and phase field distributions. For each distribution function at the boundary node, the incoming distribution from direction $\bar{i}$ (the opposite direction of i) is reflected:

$$
\begin{aligned}
f_i\left(\boldsymbol{x}_b, t + \Delta t\right) &= f_{\bar{i}}\left(\boldsymbol{x}_b, t\right), \\
g_i\left(\boldsymbol{x}_b, t + \Delta t\right) &= g_{\bar{i}}\left(\boldsymbol{x}_b, t\right).
\end{aligned}
\tag{5.8}
$$

This ensures that the fluid at the boundary node experiences no net momentum or phase field transfer. The membrane (right boundary) will have all velocity components equal to zero, virtually acting as a no-slip boundary condition [25].

Concentration flux boundary condition

For the concentration field, the right boundary will be $\partial C_{H_2}/\partial \boldsymbol{x} = 0$, with no flux, while the left will have a constant flux. The present scheme sets total flux normal through the boundary to the projection of the first-order moment of distribution functions on the surface normal [63]. The known distribution functions are post-collision populations, while the unknown distribution functions are the post-streaming populations as

$$
\begin{aligned}
\boldsymbol{j} \cdot \boldsymbol{n} = \sum_i h_i \boldsymbol{c}_i \cdot \boldsymbol{n} &= \underbrace{\sum_{\boldsymbol{c}_i \cdot \boldsymbol{n} > 0} h_i \boldsymbol{c}_i \cdot \boldsymbol{n}}_{\text{unknown}} + \underbrace{\sum_{\boldsymbol{c}_i \cdot \boldsymbol{n} \leq 0} h_i \boldsymbol{c}_i \cdot \boldsymbol{n}}_{\text{known}}, \\
&= \sum_{\boldsymbol{c}_i \cdot \boldsymbol{n} > 0} h_i^{\text{eq}}\left(C_w, \boldsymbol{u}_{\text{w}}\right) \boldsymbol{c}_i \cdot \boldsymbol{n} + \sum_{\boldsymbol{c}_i \cdot \boldsymbol{n} \leq 0} h_i \boldsymbol{c}_i \cdot \boldsymbol{n},
\end{aligned}
\tag{5.9}
$$

where j is the flux and C_w is the unknown concentration at the wall, and the unknown populations are found by $h_i = h_i^{eq}(C_w, \boldsymbol{u}_b)$. Rearranging Eq. 5.9 and using the population arrangement shown in Figure 5.1, C_w will be given by,

$$j_x = \underbrace{-c\,(h_3 + h_6 + h_7)}_{\mathbf{c}_i \cdot \mathbf{n} \leq 0} + \underbrace{c\left(h_1^{eq} + h_5^{eq} + h_8^{eq}\right)}_{\mathbf{c}_i \cdot \mathbf{n} > 0},$$

$$j_x = -c\,(h_3 + h_6 + h_7) + c\,(w_1 C_w + w_5 C_w + w_8 C_w),$$

$$C_w = \frac{j_x + h_3 + h_6 + h_7}{w_1 + w_5 + w_8}.$$

(5.10)

The H_2 flux imposed will be $j_x = 7.9 \times 10^{-10}$mols/s, the same value that Khalighi et al. uses. Additionally, the H_2 concentration will be lowered by a factor of ten compared to the supersaturated case discussed in the previous chapter, to $49,603$ mol/m^3 in the liquid. This ensures that the constant flux of H_2 at the electrode affects the growth profile of the bubble.

5.2.1. Bubble radius and concentration boundary layer thickness

The parameters given in Table 4.1 are again used to simulate the system with a constant hydrogen flux. The domain will be the same as that of Figure 4.1 with the boundaries modified as mentioned earlier in the present chapter.

Khalighi et al. states that diffusion-controlled growth still happens even when the exponent of Eq. 4.3 is larger than 0.5. Their results show that diffusion-controlled growth occurs for values of $b = 0.8$. Bernts observed a growth exponent of $b = 0.7$ in stagnant flow, using an axisymmetric method. These results match that of Figure 5.2a where the fitted exponent of the data obtained from the present study is also $b = 0.7$. The physical time at the end of the simulation is $t = 44.95$ms, allows for a clearer visualisation of this trend, than in the case of a bubble in a supersaturated domain only, as the later was run only until 4.495ms.

The diffusive boundary layer of the electrode δ_E and the bubble δ_D are plotted in Figure 5.2b. Figure 10b in the work of Khalighi et al., the behaviour of δ_E for different conditions. While the numerical values do not compare to those seen in Figure 5.2b, the trend is comparable. Both sets of results have a concave curve where for $t < 0.02s$, the diffusive boundary layer thickness at the electrode is increasing and, for the remaining physical time, has a slightly decreasing trend.
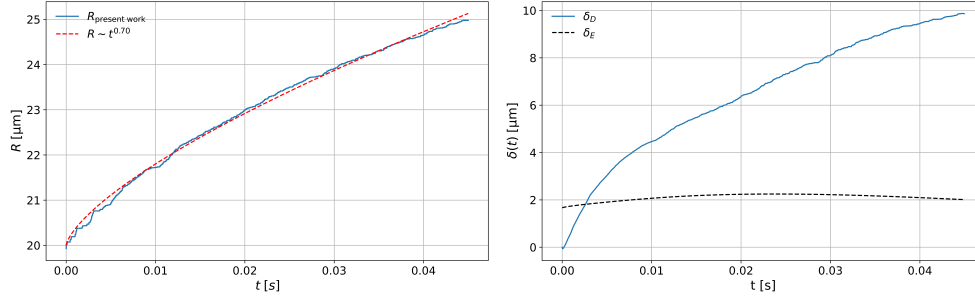
(a) Bubble growth with constant H_2 flux with $R \sim t^{0.7}$.

(b) Diffusive boundary layer thickness of the electrode δ_E and the bubble δ_D.

Figure 5.2.: Bubble radius and relevant diffusive boundary layer thickness of the system. While δ_E remains somewhat constant, δ_D increases similarly to $R(t)$.

5.2.2. Concentration profile evolution

The concentration profile evolution of the system is shown in Figure 5.3. At $t = 2.25$ms, the interface already shows an increase in the local concentration thanks to a combination of diffusion, which brings H_2 to the surface, and Henry's Law, which sets the concentration inside the bubble. The concentration boundary layer thickness at the electrode (δ_E) shows a change in shape from a constant thickness at $t = 2.25$ms to a curved, somewhat parabolic shape at $t = 44.95$ms. The parabolic profile of δ_E shown in Figure 5.2b occurs as the bubble grows, and so does δ_D. Visualy the increase in δ_D is shown in Figure 5.3, but only after $t > 11.25$ ms we see δ_D affect the instantaneous profile of δ_E. This explains the decrease in the average thickness shown in Figure 5.2b for the latter half of δ_E. At all times in the system, the diffusive boundary layer around the bubble remains radially symmetrical. Intuitively, one could expect that the region near the cathode shows a H_2 accumulation. However, the system is diffusion-limited, implying that even when the bubble is "bombarded" with H_2, the diffusion of this species will have a threshold imposed by δ_D which will only allow a limited quantity of H_2 to diffuse near the interface.
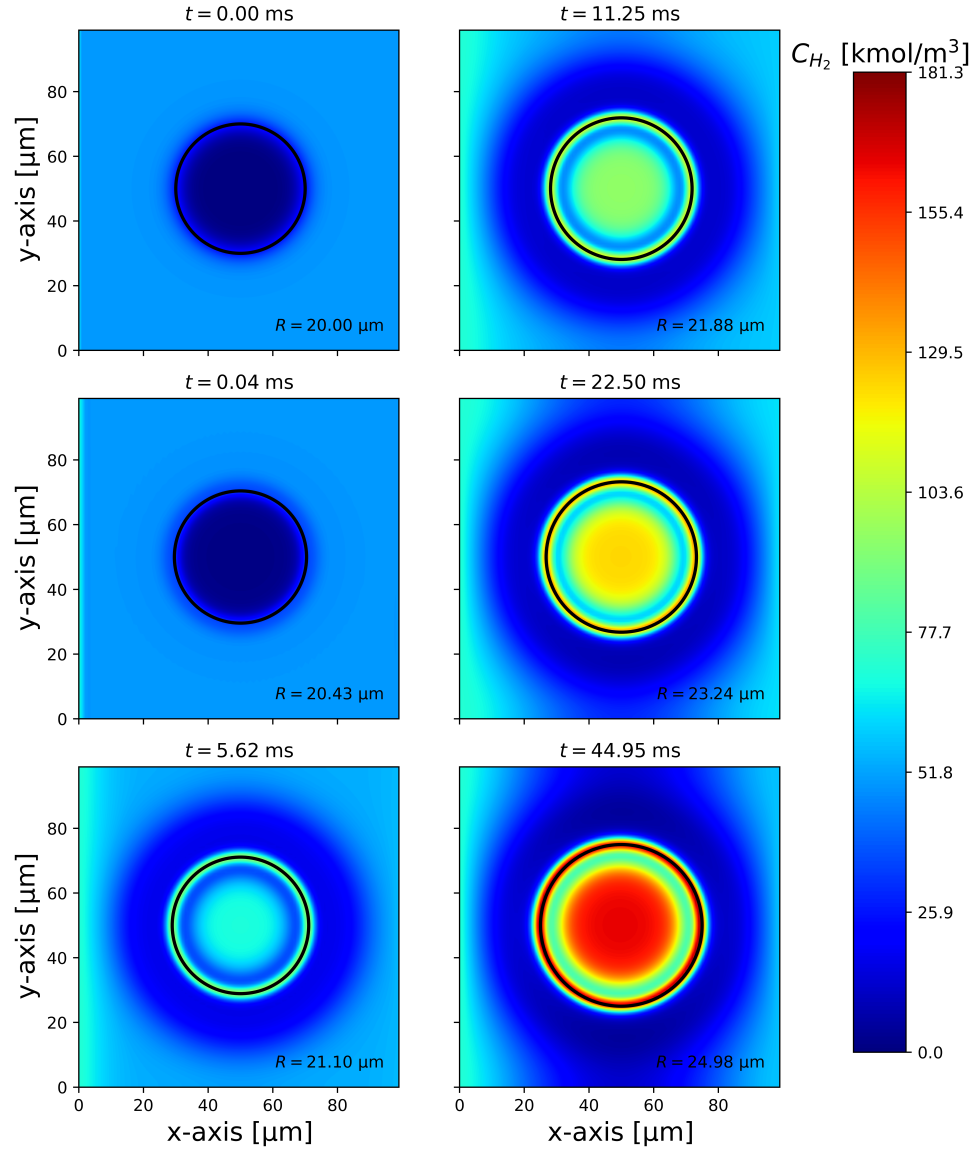
Figure 5.3.: Concentration field in kmol/m^3 for a single bubble at different times. The black circle denotes the bubble's radius.

A simulation based on fictitious physical variables was set up to show a non-diffusion-limited system. The parameters used are shown in Table 5.1. Figure 5.4 shows the con-

Table 5.1.: Parameters used for "test" simulation to prove the system is diffusion limited.

$\Delta x\,[\mu m]$	$\Delta t\,[ns]$	$R\,[\mu m]$	ρ_l/ρ_g	$D_l[m^2/s]$	$D_g[m^2/s]$	$\nu_l[m^2/s]$	$\nu_g[m^2/s]$	$\sigma[N/m]$
1	10	20	1000	1.08×10^{-6}	1.08×10^{-5}	1.45×10^{-6}	1.29×10^{-6}	0.0044

centration profile at different times. The concentration boundary layer for this case is not radially symmetrical, showing that this system is not diffusion-limited. Furthermore, an accumulation of H_2 on the left side of the bubble is observed, a characteristic not seen in Figure 5.3.
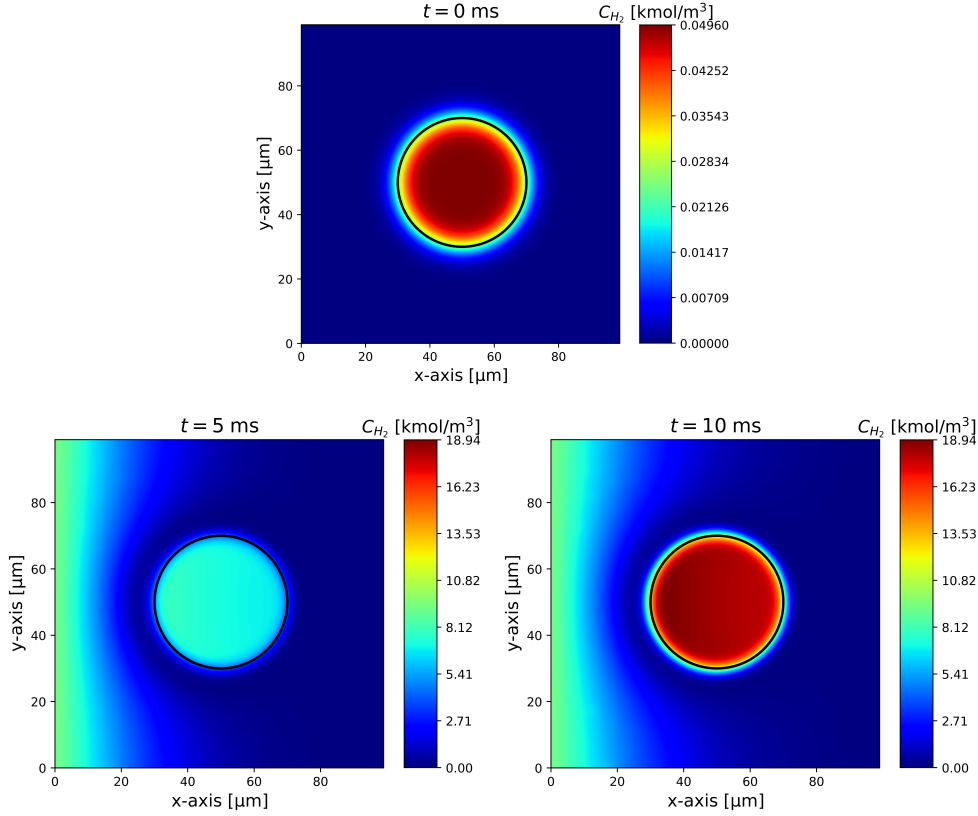
Figure 5.4.: Concentration profile for a single bubble with test physical parameters.

Figure 5.5 shows the concentration profile along the bubble at $L_y/2$ at different times. The lack of concentration accumulation at different times shows that H_2 diffuses from the bulk liquid into the gas symmetrically around the bubble. A slight difference is observed at $t = 44.95$ms. The concentration jump at the interface, a condition imposed via Henry's Law, shows an increasing tendency at later times. At $t = 2.25$ ms the average value obtained is of $He_{num} = 2.93$, while at $t = 44.95$ ms this value corresponds to $He_{num} = 16.13$. The increasing tendency shows that the system is still evolving and that the imposed value for Henry's constant has not been reached.

Figure 5.5.: Concentration profile along the centre line of the bubble cross section for a constant H_2 flux boundary condition on the electrode surface.

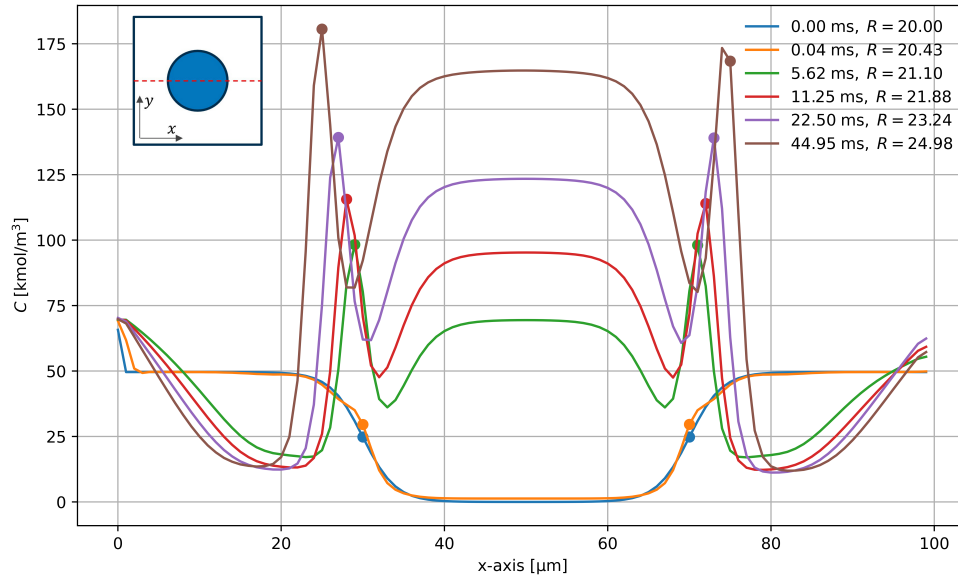The boundary layer thickness of the electrode and the bubble are also quasi-qualitatively observed in Figure 5.5. At any time, a slight difference is seen near the electrode, which resembles δ_E. The diffusive boundary layer thickness for the bubble is observed at the lower concentration regions around the bubble interface (to the left and right of the filled dots for each line); however, it is difficult to quantify from Figure 5.5, especially given the diffuse multiphase method that is being used in the present work.

Both in Figure 5.3 and Figure 5.5, a dip inside the bubble is observed right after the filled markers. This dip in concentration occurs as the bubble interface grows, and its wake leaves a region of depleted H_2. The high concentration of H_2 in the middle of the bubble then diffuses towards the depleted region as the system tries to level out the concentration gradients inside the bubble.

5.2.3. Hydrogen diffusion across the interface

To further identify the behaviour of the mass flux across the interface, the mass source term q for the phase field (Eq. 3.35) is analysed at $t = 44.95$ ms. Figure 5.6 shows a vector plot of q. The q vectors inside the bubble point towards the interface. Meanwhile, the mass source vectors at the interface that are situated just inside the bubble point towards the centre, while the vectors just outside the interface point in the opposite direction. The difference in the direction can be attributed to Equation 3.35, which is composed of two terms: the first one is driven by concentration gradients ($D_{\text{eff}} \nabla C$), while phase gradients drive the second $D_{\text{eff}} \nabla \phi$.
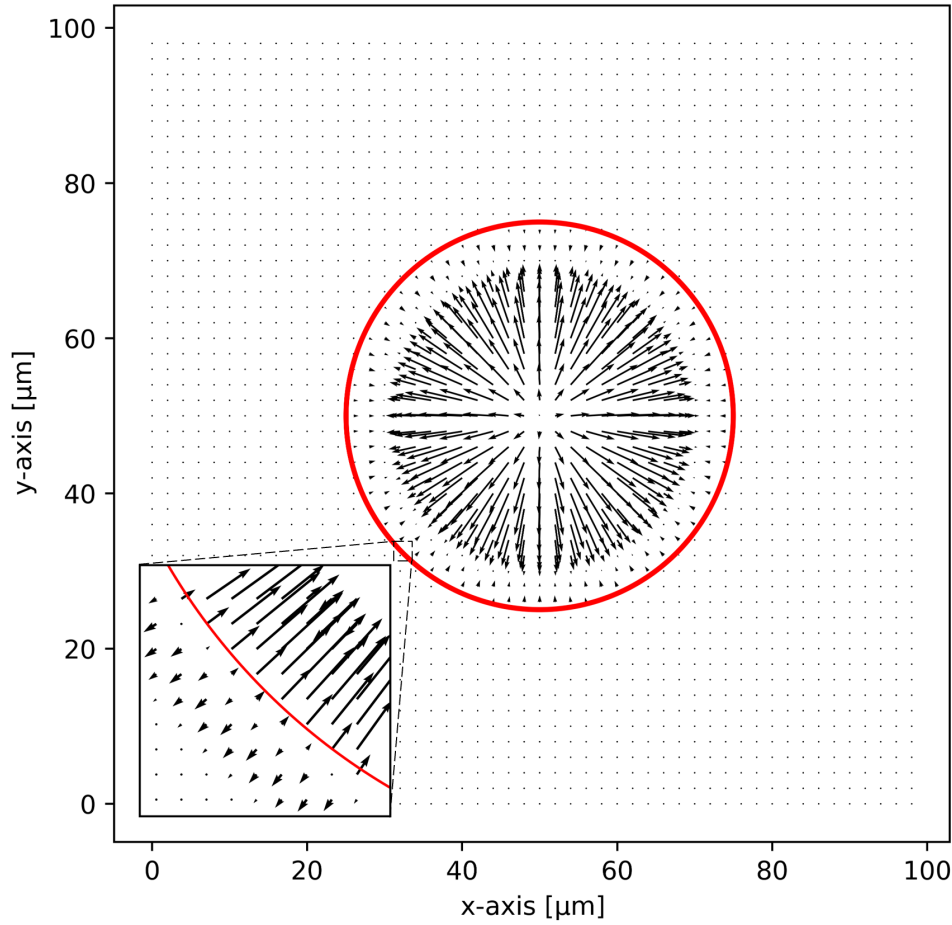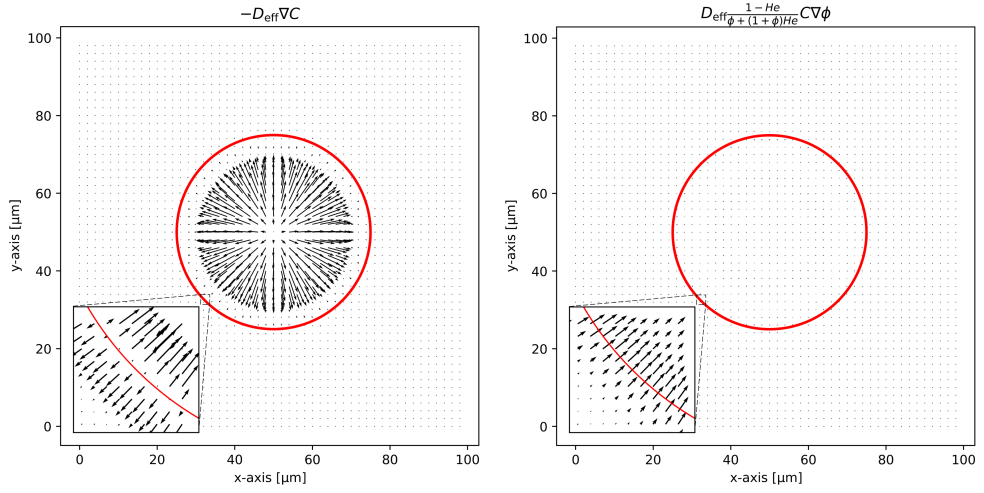
Figure 5.6.: Total mass transport vector plot for the bubble, where the red circle denotes the bubble, and the inset is a zoomed image at the interface.

Figure 5.6 can be decomposed into the concentration and phase gradient terms of Eq. 3.35, as seen in Figure 5.7. Figure 5.7a shows the behaviour of the mass because of concentration gradients. The high concentration at the bubble's centre diffuses from the centre towards the interface. However, as seen in the interface inset, the behaviour differs. From the concentration profiles shown in the previous section, it is evident that at the interface, the concentration is the highest and thus $-D_{eff}\nabla C$ points towards lower concentration regions. The depletion region of H_2 near the interface (but inside of the bubble) can be seen by the insignificant vector magnitude upholding what was said in the previous subsection.

Figure 5.7b shows the vector plot for the phase field mass transfer term. This term is responsible purely for the mass transfer across the interface. The magnitude of the vectors through the whole plot is small. However, the interface inset shows that the mass is being transported across the interface as all the vectors point towards the bubble's centre. The inset of Figure 5.7a and Figure 5.7b are both scaled by the same factor; thus, by visual inspection of the interface, the vector direction is towards the centre of the bubble. Both terms account for the additional mass that will make the bubble grow

(a) Vector plot of the concentration gradient term of the mass source term in Eq. 3.35 at $t = 44.95$ms.

(b) Vector plot of the phase gradient term of the mass source term in Eq. 3.35 at $t = 44.95$ms.

Figure 5.7.: Mass transport vector plot of the bubble. The red line denotes the bubble, and the inset denotes a zoomed-in image at the interface.

6. Conclusion and Outlook

This study aimed to implement a multiphase lattice Boltzmann method to allow for species diffusion from the liquid phase of the electrolyte into the gaseous phase, while tracking bubble growth. This goal was achieved by addressing the secondary objectives of the project sequentially.

The first step was to understand the different multiphase models in lattice Boltzmann simulations and their limitations, particularly for high-density ratio multiphase models. A single-component Shan-Chen, a Colour Gradient with enhanced equilibria, and a Phase-Field method were implemented in Python and compared. The Shan-Chen method confirmed the density ratio dependency on the strength of the molecular interaction $G_{k\bar{k}}$. While simple to implement and computationally efficient, the Shan-Chen SCMP simulation could only reach two orders of magnitude of the density ratio and exhibited large spurious velocities. The Colour Gradient with enhanced equilibria appeared to be an attractive solution for this study, as it could adequately capture the pressure jump across the interface and allow for independent surface tension tuning, aiding in simulating static bubbles with up to three orders of magnitude. However, the downside of the Colour Gradient scheme was the challenge of implementing a mass transport term dependent on the concentration field, which remains an area of ongoing research. Lastly, the Phase-Field interface tracking SCMP model developed by Zheng et al. was initially validated using the Laplace law, similar to the Colour Gradient method. The results showed less deviation from the analytical solution than the Colour Gradient and had smaller spurious velocities. Although the Phase-Field method was computationally expensive, it produced the best results of the three models, and Zheng et al. had already developed a coupling between the concentration, pressure, and phase field, enabling mass transfer from the gas to the liquid phase.

The analytical solution of the *Sh* proposed by Newman validates the coupling of concentration, pressure, and phase distribution functions. The results qualitatively matched those of Zheng et al., correctly solving continuous species transfer. This was followed by a simulation of a growing H_2 bubble in a supersaturated domain. Due to the large diffusivity ratios of up to four orders of magnitude, an MRT scheme for the concentration field was developed. Even with the MRT scheme, instabilities were observed, highlighting the importance of adequately assigning spatial and temporal conversion factors. Nevertheless, diffusion-controlled bubble growth $\left(R \sim bt^{0.5}\right)$ was observed, as reported in the literature [25]. The assumption of thermal equilibrium at the interface posed a challenge, as it required the system to first reach equilibrium to correctly determine whether the imposed *He* would be achieved, affecting the system's pressure. A three-dimensional version of the Phase-Field interface tracking model was implemented with a D3Q19 velocity set to simulate bubble growth. However, its computational cost was extremely high, making it infeasible for further development in this study.

The next logical step was to implement a constant flux of H_2 at one of the domain's boundaries to analyse bubble growth in a supersaturated domain. A wet node approach was chosen, which determined the concentration at the boundary (electrode) using known and

unknown populations [63]. The bubble growth exponent increased from 0.5 to 0.7 when the left boundary has a constant hydrogen flux. The presence of H_2 flux at the electrode introduced a diffusive boundary layer near the surface, which grew until the bubble's diffusive boundary layer began affecting that of the electrode. The condition of imposing a constant flux of H_2 implies that the system will never reach equilibrium as, meaning that the bubble will grow continuously. This simulation, run at a low spatial resolution (1X), took over a week to simulate 45 ms of physical time, demonstrating the need for parallelisation of the code.

The saturated hydrogen concentration for the conditions of the system is 0.16 mol/m^3. This value is given as the initial concentration for the bubble, while substantial concentration values are given as the initial condition for the liquid. While unphysical, the values given to the liquid are essential for the present work since they ensured that bubble growth is observed for shorter times due to the large concentration gradients. However, the upside of using vast concentration differences between the liquid and gaseous phases is that the method proved to handle it appropriately, showing that the implementation of an MRT collision operator in the concentration distribution is adequate.

6.1. Outlook

Due to the limited time and scope of the present study, the relevant electrochemical physics of alkaline water electrolysis was not thoroughly analysed. Additionally, parallelising the code in Python or using an open-source platform should be considered. Another recommendation is to explore the extension of mass transport in other multiphase models, such as the Colour Gradient.

6.1.1. Poisson-Nernst-Planck coupling

The transport mechanism of all species: H_2, H_2O, OH^- and K^+ has not been resolved in this study. Extending this to a MCMP model is feasible using the current Phase-Field interface tracking model by adding a Poisson-Nernst-Planck coupling. Models such as those developed by Murugesan [10] would provide deeper insight into the electrochemical production of hydrogen at the cathode and the species transport dynamics in AWE. Other physical phenomena like detachment are important realistic phenomenology that have not been investigated in the present work, which should also be considered for future work. Bubble coalescence, another important physical process, while not analysed, can be realised with the current LB multiphase method. All of the suggestions above would significantly increase computational costs, making parallel computing essential for further development.

6.1.2. Parallel computing

The lattice Boltzmann Method, at the mesoscale, outperforms traditional methods such as Finite Volume and Finite Differences, especially when dealing with MCMP electrochemical systems, such as the analysed in this study. The downside of the LBM is its significant memory requirements with higher velocity set stencils. However, one key advantage of LBM is that the discretisation of individual particles can be handled simultaneously using

multiple CPU or GPU cores, significantly speeding up calculations. Its highly localised update process, requiring information only from neighbouring nodes, makes it particularly efficient for parallel processing in shared and distributed memory systems. Open-source codes such as LBPM for porous media, a robust C++ code with many physical models implemented, enable CPU and GPU multi-core calculations and should be the next extension of the current model.

6.1.3. Colour Gradient mass transfer implementation

Currently, there is a research gap in the development of Colour Gradient methods that involve mass transfer from a liquid phase into a gaseous phase or vice versa. Mora et al. developed a model to simulate two-phase flow with a new distribution function to model the concentration profile of a substance. While not entirely analogous to the current study, it could serve as a foundation for further implementation of a mass transfer term in the Colour Gradient multiphase model. Implementing this in the Colour Gradient model is promising due to its ability to handle large viscosity ratios, a wide range of surface tensions, and its accuracy and convenience in setting the wetting angle.

Bibliography

[1] Lin Zheng, Taehun Lee, Zhaoli Guo, and David Rumschitzki. Shrinkage of bubbles and drops in the lattice boltzmann equation method for nonideal gases. *Phys. Rev. E*, 89:033302, Mar 2014. doi: 10.1103/PhysRevE.89.033302. URL https://link.aps.org/doi/10.1103/PhysRevE.89.033302.

[2] European Council. How is eu electricity produced and sold?, May 2023. URL https://www.consilium.europa.eu/en/infographics/how-is-eu-electricity-produced-and-sold/.

[3] International Energy Agency (IEA). The future of hydrogen. Technical report, IEA, Paris, 2019. URL https://www.iea.org/reports/the-future-of-hydrogen. License: CC BY 4.0.

[4] Ali Keçebaş, Muhammet Kayfeci, and Mutlucan Bayat. Chapter 9 - electrochemical hydrogen generation. In Francesco Calise, Massimo Dentice D'Accadia, Massimo Santarelli, Andrea Lanzini, and Domenico Ferrero, editors, *Solar Hydrogen Production*, pages 299–317. Academic Press, 2019. ISBN 978-0-12-814853-2. doi: https://doi.org/10.1016/B978-0-12-814853-2.00009-6. URL https://www.sciencedirect.com/science/article/pii/B9780128148532000096.

[5] M. Chatenet, B. G. Pollet, D. R. Dekel, F. Dionigi, J. Deseure, P. Millet, R. D. Braatz, M. Z. Bazant, M. Eikerling, I. Staffell, P. Balcombe, Y. Shao-Horn, and H. Schäfer. Water electrolysis: from textbook knowledge to the latest scientific strategies and industrial developments. *Chemical Society Reviews*, 51(11):4583–4762, 2022. doi: 10.1039/d0cs01079k. URL https://doi.org/10.1039/d0cs01079k.

[6] Jude Olaoluwa-Majasan. *Investigation of Mass Transport Phenomena in Polymer Electrolyte Membrane Water Electrolysers*. PhD thesis, University College of London, 2019.

[7] Yangyang Li, Tao Zhang, Xintao Deng, Biao Liu, Jugang Ma, Fuyuan Yang, and Minggao Ouyang. Active pressure and flow rate control of alkaline water electrolyzer based on wind power prediction and 100 *Applied Energy*, 328:120172, 2022. ISSN 0306-2619. doi: https://doi.org/10.1016/j.apenergy.2022.120172. URL https://www.sciencedirect.com/science/article/pii/S0306261922014295.

[8] Sergey A. Grigoriev, Vladimir N. Fateev, and Pierre Millet. 4.18 - alkaline electrolysers. In Trevor M. Letcher, editor, *Comprehensive Renewable Energy (Second Edition)*, pages 459–472. Elsevier, Oxford, second edition edition, 2022. ISBN 978-0-12-819734-9. doi: https://doi.org/10.1016/B978-0-12-819727-1.00024-8. URL https://www.sciencedirect.com/science/article/pii/B9780128197271000248.

[9] D. Santos, César Sequeira, and José Figueiredo. Hydrogen production by alkaline water electrolysis. *Química Nova*, 36:1176–1193, 12 2012. doi: 10.1590/S0100-40422013000800017.

[10] Vikki Murugesan. Multi-species electrochemical reaction modeling using lattice boltz-mann method: study of transport phenomena in alkaline water electrolyzer. Master's thesis, Delft University of Technology, 8 2023. URL http://resolver.tudelft.nl/uuid:6f143cfa-dec7-47a0-a622-e5e780a8dfe0.

[11] Yang Liu, Shuang Li, Honglu Wu, and Yixiang Shi. Experimental investigation and analysis for the bubble size distribution during alkaline water electrolysis by using a wire electrode. *DeCarbon*, 5:100052, 2024. ISSN 2949-8813. doi: https://doi.org/10.1016/j.decarb.2024.100052. URL https://www.sciencedirect.com/science/article/pii/S2949881324000180.

[12] Sunghak Park, Luhao Liu, Çayan Demirkır, Onno van der Heijden, Detlef Lohse, Dominik Krug, and Marc T. M. Koper. Solutal marangoni effect determines bub-ble dynamics during electrocatalytic hydrogen evolution. *Nature Chemistry*, 15(11): 1532–1540, 2023. doi: 10.1038/s41557-023-01294-y. URL https://doi.org/10.1038/s41557-023-01294-y.

[13] K. Zeng and Dongke Zhang. Recent progress in alkaline water electrolysis for hydrogen production and applications. *Progress in Energy and Combustion Science: an international review journal*, 36:307–326, 2010. ISSN 0360-1285. doi: 10.1016/j.pecs.2009.11.002.

[14] R.M. de Jonge, E. Barendrecht, L.J.J. Janssen, and S.J.D. van Stralen. Gas bubble be-haviour and electrolyte resistance during water electrolysis. *International Journal of Hy-drogen Energy*, 7(11):883–894, 1982. ISSN 0360-3199. doi: https://doi.org/10.1016/0360-3199(82)90007-6. URL https://www.sciencedirect.com/science/article/pii/0360319982900076.

[15] N. Nagai, M. Takeuchi, T. Kimura, and T. Oka. Existence of optimum space be-tween electrodes on hydrogen production by water electrolysis. *International Jour-nal of Hydrogen Energy*, 28(1):35–41, 2003. ISSN 0360-3199. doi: https://doi.org/10.1016/S0360-3199(02)00027-7. URL https://www.sciencedirect.com/science/article/pii/S0360319902000277.

[16] A. Bashkatov, A. Babich, S.S. Hossain, X. Yang, G. Mutschke, and K. Eckert. H2 bubble motion reversals during water electrolysis. *Journal of Fluid Mechanics*, 958:A43, 2023. doi: 10.1017/jfm.2023.91.

[17] Xiaohan Mei, Shu Yuan, Congfan Zhao, Xiaohui Yan, ChangYing Zhao, and Qian Wang. Measuring three-dimensional bubble dynamics for hydrogen production via water electrolysis. *Physics of Fluids*, 35(12):123338, 12 2023. ISSN 1070-6631. doi: 10.1063/5.0173622. URL https://doi.org/10.1063/5.0173622.

[18] Sébastien Leclaire, Marcelo Reggio, and Jean-Yves Trépanier. Numerical evaluation of two recoloring operators for an immiscible two-phase flow lattice boltzmann model. *Applied Mathematical Modelling*, 36(5):2237–2252, 2012. ISSN 0307-904X. doi: https://doi.org/10.1016/j.apm.2011.08.027. URL https://www.sciencedirect.com/science/article/pii/S0307904X11005270.

[19] Zhikai Tan, Hongjie Yan, Rongzong Huang, Liu Liu, and Qing Li. Phase-field lattice boltzmann method for the simulation of gas-liquid mass transfer. *Chemi-cal Engineering Science*, 253:117539, 2022. ISSN 0009-2509. doi: https://doi.org/10.1016/j.ces.2022.117539. URL https://www.sciencedirect.com/science/article/pii/S0009250922001233.

[20] Karun Pravin Nirod Datadien. *Directional instabilities in microdroplet jetting: a numerical approach*. Phd thesis 1 (research tu/e / graduation tu/e), Applied Physics and Science Education, January 2024. Proefschrift.

[21] Z.L. Yang, T.N. Dinh, R.R. Nourgaliev, and B.R. Sehgal. Numerical investigation of bubble growth and detachment by the lattice-boltzmann method. *International Journal of Heat and Mass Transfer*, 44(1):195–206, 2001. ISSN 0017-9310. doi: https://doi.org/10.1016/S0017-9310(00)00101-0. URL https://www.sciencedirect.com/science/article/pii/S0017931000001010.

[22] Shuyong Chen, Bo Fu, Xigang Yuan, Huishu Zhang, Wei Chen, and Kuotsung Yu. Lattice boltzmann method for simulation of solutal interfacial convection in gas–liquid system. *Industrial & Engineering Chemistry Research*, 51(33):10955–10967, 2012. doi: 10.1021/ie3018912. URL https://doi.org/10.1021/ie3018912.

[23] Shubhani Paliwal, Debashis Panda, Supriya Bhaskaran, Nicole Vorhauer-Huget, Evangelos Tsotsas, and Vikranth Kumar Surasani. Lattice boltzmann method to study the water-oxygen distributions in porous transport layer (ptl) of polymer electrolyte membrane (pem) electrolyser. *International Journal of Hydrogen Energy*, 46(44):22747–22762, 2021. ISSN 0360-3199. doi: https://doi.org/10.1016/j.ijhydene.2021.04.112. URL https://www.sciencedirect.com/science/article/pii/S0360319921015007.

[24] Ethan Young, Arth Sojitra, Jacob Wrubel, and Marc Henry de Frahan. A lattice boltzmann method for predicting porous transport layer performance during electrolysis. 9 2023. URL https://www.osti.gov/biblio/1999381.

[25] Faeze Khalighi, Niels G. Deen, Yali Tang, and Albertus W. Vreman. Hydrogen bubble growth in alkaline water electrolysis: An immersed boundary simulation study. *Chemical Engineering Science*, 267:118280, 2023. ISSN 0009-2509. doi: https://doi.org/10.1016/j.ces.2022.118280. URL https://www.sciencedirect.com/science/article/pii/S000925092200865X.

[26] N. P. Brandon and G. H. Kelsall. Growth kinetics of bubbles electrogenerated at microelectrodes. *Journal of Applied Electrochemistry*, 15(4):475–484, 1985. doi: 10.1007/BF01059288. URL https://doi.org/10.1007/BF01059288.

[27] Emily M. Ryan and Partha P. Mukherjee. Mesoscale modeling in electrochemical devices—a critical perspective. *Progress in Energy and Combustion Science*, 71:118–142, 2019. ISSN 0360-1285. doi: https://doi.org/10.1016/j.pecs.2018.11.002. URL https://www.sciencedirect.com/science/article/pii/S0360128518300078.

[28] Sicilia Ferreira Judice. *Lattice Boltzmann Method for Fluid Simulation*, pages 1–10. Springer International Publishing, Cham, 2018. ISBN 978-3-319-08234-9. doi: 10.1007/978-3-319-08234-9_107-1. URL https://doi.org/10.1007/978-3-319-08234-9_107-1.

[29] P. L. Bhatnagar, E. P. Gross, and M. Krook. A model for collision processes in gases. i. small amplitude processes in charged and neutral one-component systems. *Phys. Rev.*, 94:511–525, May 1954. doi: 10.1103/PhysRev.94.511. URL https://link.aps.org/doi/10.1103/PhysRev.94.511.

[30] Y. H. Qian, D. D'Humières, and P. Lallemand. Lattice bgk models for navier-stokes equation. *Europhysics Letters*, 17(6):479, feb 1992. doi: 10.1209/0295-5075/17/6/001. URL https://dx.doi.org/10.1209/0295-5075/17/6/001.

[31] Timm Krüger, Halim Kusumaatmaja, Alexandr Kuzmin, Orest Shardt, Goncalo Silva, and Erlend Magnus Viggen. *The Lattice Boltzmann Method*. Graduate Texts in Physics. Springer, Cham, first edition, 2017. ISBN 978-3-319-83103-9. doi: 10.1007/978-3-319-44649-3. URL https://link.springer.com/book/10.1007/978-3-319-44649-3.

[32] Zhaoli Guo, Chuguang Zheng, and Baochang Shi. Discrete lattice effects on the forcing term in the lattice boltzmann method. *Physical review. E, Statistical, nonlinear, and soft matter physics*, 65:046308, 05 2002. doi: 10.1103/PhysRevE.65.046308.

[33] AA Mohamad and AA Mohamad. The boltzmann equation. *Lattice Boltzmann method: fundamentals and engineering applications with computer codes*, pages 15–24, 2011.

[34] Xiyun Lu Haibo Huang, Michael Sukop. *Introduction*, chapter 1-10, pages 1–358. John Wiley and Sons, Ltd, 2015. ISBN 9781118971451. doi: https://doi.org/10.1002/9781118971451.ch1. URL https://onlinelibrary.wiley.com/doi/abs/10.1002/9781118971451.ch1.

[35] Like Li, Renwei Mei, and James F. Klausner. Lattice boltzmann models for the convection-diffusion equation: D2q5 vs d2q9. *International Journal of Heat and Mass Transfer*, 108:41–62, 2017. ISSN 0017-9310. doi: https://doi.org/10.1016/j.ijheatmasstransfer.2016.11.092. URL https://www.sciencedirect.com/science/article/pii/S0017931016326047.

[36] Mayken Espinoza-Andaluz, Ayrton Moyón, and Martin Andersson. A comparative study between d2q9 and d2q5 lattice boltzmann scheme for mass transport phenomena in porous media. *Computers and Mathematics with Applications*, 78(9):2886–2896, 2019. ISSN 0898-1221. doi: https://doi.org/10.1016/j.camwa.2019.02.012. URL https://www.sciencedirect.com/science/article/pii/S089812211930080X. Applications of Partial Differential Equations in Science and Engineering.

[37] Irina Ginzburg, Dominique Dhumieres, and Alexander Kuzmin. Optimal stability of advection-diffusion lattice boltzmann models with two relaxation times for positive/negative equilibrium. *Journal of Statistical Physics*, 139:1090–1143, 06 2010. doi: 10.1007/s10955-010-9969-9.

[38] X. D. Niu, C. Shu, Y. T. Chew, and T. G. Wang. Investigation of stability and hydrodynamics of different lattice boltzmann models. *Journal of Statistical Physics*, 117(3):665–680, 11 2004. ISSN 1572-9613. doi: 10.1007/s10955-004-2264-x. URL https://doi.org/10.1007/s10955-004-2264-x.

[39] Daryl Grunau, Shiyi Chen, and Kenneth Eggert. A lattice Boltzmann model for multiphase fluid flows. *Physics of Fluids A: Fluid Dynamics*, 5(10):2557–2562, 10 1993. ISSN 0899-8213. doi: 10.1063/1.858769. URL https://doi.org/10.1063/1.858769.

[40] Xiaowen Shan and Hudong Chen. Lattice boltzmann model for simulating flows with multiple phases and components. *Phys. Rev. E*, 47:1815–1819, Mar 1993. doi: 10.1103/PhysRevE.47.1815. URL https://link.aps.org/doi/10.1103/PhysRevE.47.1815.

[41] Michael R. Swift, W. R. Osborn, and J. M. Yeomans. Lattice boltzmann simulation of nonideal fluids. *Phys. Rev. Lett.*, 75:830–833, Jul 1995. doi: 10.1103/PhysRevLett.75.830. URL https://link.aps.org/doi/10.1103/PhysRevLett.75.830.

[42] Xiaowen Shan and Gary Doolen. Multicomponent lattice-boltzmann model with interparticle interaction. *Journal of Statistical Physics*, 81(1):379–393, 10 1995. ISSN 1572-9613. doi: 10.1007/BF02179985. URL https://doi.org/10.1007/BF02179985.

[43] M. Sbragaglia and X. Shan. Consistent pseudopotential interactions in lattice boltzmann models. *Phys. Rev. E*, 84:036703, Sep 2011. doi: 10.1103/PhysRevE.84.036703. URL https://link.aps.org/doi/10.1103/PhysRevE.84.036703.

[44] Marcello Sega, Mauro Sbragaglia, Sofia S. Kantorovich, and Alexey O. Ivanov. Mesoscale structures at complex fluid–fluid interfaces: a novel lattice boltzmann/-molecular dynamics coupling. *Soft Matter*, 9:10092–10107, 2013. doi: 10.1039/C3SM51556G. URL http://dx.doi.org/10.1039/C3SM51556G.

[45] Sébastien Leclaire, Andrea Parmigiani, Orestis Malaspinas, Bastien Chopard, and Jonas Latt. Generalized three-dimensional lattice boltzmann color-gradient method for immiscible two-phase pore-scale imbibition and drainage in porous media. *Phys. Rev. E*, 95:033306, Mar 2017. doi: 10.1103/PhysRevE.95.033306. URL https://link.aps.org/doi/10.1103/PhysRevE.95.033306.

[46] M. Latva-Kokko and Daniel H. Rothman. Diffusion properties of gradient-based lattice boltzmann models of immiscible fluids. *Phys. Rev. E*, 71:056702, May 2005. doi: 10.1103/PhysRevE.71.056702. URL https://link.aps.org/doi/10.1103/PhysRevE.71.056702.

[47] T Reis and T N Phillips. Lattice boltzmann model for simulating immiscible two-phase flows. *Journal of Physics A: Mathematical and Theoretical*, 40(14):4033, mar 2007. doi: 10.1088/1751-8113/40/14/018. URL https://dx.doi.org/10.1088/1751-8113/40/14/018.

[48] Abbas Fakhari, Martin Geier, and Taehun Lee. A mass-conserving lattice boltzmann method with dynamic grid refinement for immiscible two-phase flows. *Journal of Computational Physics*, 315:434–457, 2016. ISSN 0021-9991. doi: https://doi.org/10.1016/j.jcp.2016.03.058. URL https://www.sciencedirect.com/science/article/pii/S0021999116300237.

[49] Julien Maes and Cyprien Soulaine. A unified single-field volume-of-fluid-based formulation for multi-component interfacial transfer with local volume changes. *Journal of Computational Physics*, 402:109024, 2020. ISSN 0021-9991. doi: https://doi.org/10.1016/j.jcp.2019.109024. URL https://www.sciencedirect.com/science/article/pii/S0021999119307302.

[50] Maximilian Schalenbach, Wiebke Lueke, and Detlef Stolten. Hydrogen diffusivity and electrolyte permeability of the zirfon perl separator for alkaline water electrolysis. *Journal of The Electrochemical Society*, 163(14):F1480, oct 2016. doi: 10.1149/2.1251613jes. URL https://dx.doi.org/10.1149/2.1251613jes.

[51] Sumesh P. Thampi, Santosh Ansumali, R. Adhikari, and Sauro Succi. Isotropic discrete laplacian operators from lattice hydrodynamics. *Journal of Computational Physics*, 234:1–7, 2013. ISSN 0021-9991. doi: https://doi.org/10.1016/j.jcp.2012.07.037. URL https://www.sciencedirect.com/science/article/pii/S0021999112004226.

[52] Haihu Liu, Qinjun Kang, Christopher R. Leonardi, Sebastian Schmieschek, Ariel Narváez, Bruce D. Jones, John R. Williams, Albert J. Valocchi, and Jens Harting. Multiphase lattice boltzmann simulations for porous media applications. *Computational Geosciences*, 20(4):777–805, 2016. ISSN 1573-1499. doi: 10.1007/s10596-015-9542-3.

[53] Andrea Angulo, Peter van der Linde, Han Gardeniers, Miguel Modestino, and David Fernández Rivas. Influence of bubbles on the energy conversion efficiency of electrochemical reactors. *Joule*, 4(3):555–579, 2020. ISSN 2542-4351. doi: https://doi.org/10.1016/j.joule.2020.01.005. URL https://www.sciencedirect.com/science/article/pii/S2542435120300325.

[54] AB Newman. The drying of porous solid. diffusion and surface emission effects. *Trans. AIChE*, 27(203-216), 1931.

[55] D. Colombet, D. Legendre, A. Cockx, and P. Guiraud. Mass or heat transfer inside a spherical gas bubble at low to moderate reynolds number. *International Journal of Heat and Mass Transfer*, 67:1096–1105, 2013. ISSN 0017-9310. doi: https://doi.org/10.1016/j.ijheatmasstransfer.2013.08.069. URL https://www.sciencedirect.com/science/article/pii/S001793101300731X.

[56] M S Plesset and A Prosperetti. Bubble dynamics and cavitation. *Annual Review of Fluid Mechanics*, 9(Volume 9, 1977):145–185, 1977. ISSN 1545-4479. doi: https://doi.org/10.1146/annurev.fl.09.010177.001045. URL https://www.annualreviews.org/content/journals/10.1146/annurev.fl.09.010177.001045.

[57] W. K. Lewis and W. G. Whitman. Principles of gas absorption. *Industrial & Engineering Chemistry*, 16(12):1215–1220, 1924. doi: 10.1021/ie50180a002. URL https://doi.org/10.1021/ie50180a002.

[58] Mark A. Eiteman. Interlude: Interphase mass transfer, 2012. URL https://cmbe.engr.uga.edu/bche3180/Mass%20Transfer%20Coefficients.pdf.

[59] Patrick D. Sinko, Louis Parker, Lisa Prahl Wittberg, and Christel A.S. Bergström. Estimation of the concentration boundary layer adjacent to a flat surface using computational fluid dynamics. *International Journal of Pharmaceutics*, 653:123870, 2024. ISSN 0378-5173. doi: https://doi.org/10.1016/j.ijpharm.2024.123870. URL https://www.sciencedirect.com/science/article/pii/S0378517324001042.

[60] Sohail Ahmed Memon. *Mathematical modelling of complex dynamics*. PhD thesis, University of Central Lancashire, April 2017. URL https://clok.uclan.ac.uk/20497/. Unpublished.

[61] K. Oldham and J. Myland. *Fundamentals of Electrochemical Science*. Elsevier Science, 1994. ISBN 9780125255455. URL https://books.google.nl/books?id=wq8PAQAAMAAJ.

[62] Xiaoyi He and Li-Shi Luo. Lattice boltzmann model for the incompressible navier–stokes equation. *Journal of Statistical Physics*, 88(3):927–944, 1997. doi: 10.1023/B:JOSS.0000015179.12689.e4. URL https://doi.org/10.1023/B:JOSS.0000015179.12689.e4.

[63] Wende Li, Xu Su, Alan Palazzolo, and Shehab Ahmed. A flux boundary scheme in the lattice boltzmann method and its applications in the simulation of membrane desalination. *Desalination and Water Treatment*, 161:76–91, 2019. ISSN 1944-3986. doi: https://doi.org/10.5004/dwt.2019.24227. URL https://www.sciencedirect.com/science/article/pii/S1944398624155981.

[64] B. W. J. Bernts. Bubble growth in alkaline electrolysis. Master's thesis, Eindhoven University of Technology, February 2022. URL https://research.tue.nl/en/studentTheses/bubble-growth-in-alkaline-electrolysis. Date of Award: 17 Feb 2022.

[65] Peter Mora, Gabriele Morra, Dave Yuen, Shirish Patil, and Ruben Juanes. Convection-diffusion with the colour gradient lattice boltzmann method for three-component, two-phase flow. *Transport in Porous Media*, 147:1–22, 02 2023. doi: 10.1007/s11242-023-01906-8.

[66] J. Newman and K.E. Thomas-Alyea. *Electrochemical Systems*. The ECS Series of Texts and Monographs. Wiley, 2004. ISBN 9780471477563. URL https://books.google.nl/books?id=vArZu0HM-xYC.

[67] Nian-Tzu Suen, Sung-Fu Hung, Quan Quan, Nan Zhang, Yi-Jun Xu, and Hao Ming Chen. Electrocatalysis for the oxygen evolution reaction: recent development and future perspectives. *Chem. Soc. Rev.*, 46:337–365, 2017. doi: 10.1039/C6CS00328A. URL http://dx.doi.org/10.1039/C6CS00328A.

[68] John Dukovic and Charles W. Tobias. The influence of attached bubbles on potential drop and current distribution at gas-evolving electrodes. *Journal of The Electrochemical Society*, 134(2):331, feb 1987. doi: 10.1149/1.2100456. URL https://dx.doi.org/10.1149/1.2100456.

A. LBM multiphase model qualitative comparison

Table A.1.: Summary of advantages and disadvantages of lattice Boltzmann multiphase models.

Model	Advantages	Disadvantages
Colour Gradient (RK)	- Accurate - Efficient - Allows specification of wetting condition - Can achieve density ratios up to $O(10^3)$	- Mathematical instabilities in dynamic simulations - High computational cost
Shan-Chen (SC)	- Very efficient - Can achieve density ratios up to $O(10^3)$ - Allows specification of wetting condition	- Less accurate than other models - Large spurious velocities - Adjustment of parameters needed for accuracy
Free-Energy (FE)	- Accurate - Thermodynamically consistent - No wetting condition required - Interface thickness tunable	- Not efficient for multiphase systems - Limited density ratio ($O(10)$) - Spurious velocities due to surface tension
Interface Tracking (HCZ)	- Accurate - Can simulate density ratios up to $O(10^3)$ - Small spurious velocities	- Complex implementation - High computational cost - Dissolution of small droplets/bubbles

B. Electrochemistry basics in AWE

B.1. Thermodynamics and Potentials

To evaluate electrochemical systems, as well as most other reactions, the Gibbs free energy is very useful as it provides a criterion for predicting the direction of chemical or electrochemical reactions and the composition of the system under conditions of constant pressure and temperature. To measure the potential energy that exists within a system, electrochemical potentials are used as these measure the distribution of electric charge and charge separation across the system. In a half-cell, randomly assigned the sub index of 1 and 2 to the other, electrochemical potentials are used to determine the energy change due to the reaction in the system through change in the system Gibbs free energy ΔG:

$$\Delta G = \left(\sum_i s_i \mu_i \right)_1 - \left(\sum_i s_i \mu_i \right)_2 , \tag{B.1}$$

where μ_i is the electrochemical potential of species i and s_i is its stoichiometric coefficient. The Gibbs free energy of a system in which no current flows is determined via Eq. B.2, where U is the potential at which no current flows and is known as equilibrium or open-circuit potential and F is the Faraday constant which has a value of $F = 96.4853$ kCmol^{-1}. The equilibrium potential is related to the Gibbs Free energy by [66]:

$$\Delta G = -nFU, \tag{B.2}$$

where n is the number of moles of transferred electrons. The equilibrium potential is thus a function of the intrinsic nature of the species present, as well as their concentrations and, to a lesser extent, temperature. The electrochemical potential can be related to the molality m_i and activity coefficient γ_i by [66],

$$\mu_i = \mu_i^{\ominus} + R_u T \ln m_i \gamma_i, \tag{B.3}$$

where $\mu_i^{\ominus}$ is a reference electrochemical potential independent of concentration, R_u is the universal gas constant $(8.3143$ J/mol $\cdot$ K$)$, and T is temperature in kelvin. Assuming the systems behave ideally (i.e. all activity coefficients are unity), the potential U can be found, from a reference potential $U^{\ominus}$, by re-arranging Eq. B.2 to find a relation between the concentrations of the reactant and products [66],

$$U = U^{\ominus} - \frac{R_u T}{nF} \ln \left(\prod_i m_i^{s_i} \right)_1 + \frac{R_u T}{nF} \ln \left(\prod_i m_i^{s_i} \right)_2 . \tag{B.4}$$

By connecting an electrode to an external power source, the electrochemical potential of electrons within the electrode can be controlled, disrupting equilibrium and prompting a reaction. Applying a negative potential increases electron energy, leading to a reduction of

species in the adjacent electrolyte, occurring at the cathode. Conversely, a positive potential decreases electron energy, causing oxidation at the anode, where electrons are transferred from the reactants to the electrode. Applying a positive potential drives the reaction toward oxidation, while a negative potential drives it toward reduction.

In AWE at 1 bar and 25°C operating conditions, the free energy values for the anode, cathode, and the overall cell are

$$\Delta G_{anode} = 77.4 \text{ kJ/mol}, \quad \Delta G_{cathode} = -159.8 \text{ kJ/mol}, \quad \Delta G_{cell} = 237.2 \text{ kJ/mol}.$$

Hence, 237.2 kJ/mol is the minimum energy required for hydrogen production. At these operating conditions the electrode reaction is inherently slower and an over-potential η which is above the equilibrium cell potential is essential. The over-potential enables to start off the reaction surmounting the activation energy barrier, thereby increasing the reaction rate [67].

B.2. Kinetics and Rates of Reaction

A driving force is essential for initiating an electrochemical reaction, known as the surface overpotential η_s. The macroscopic relation that exists between the current density, surface overpotential, and composition of the electrolytic solution near the electrode surface is of paramount importance [61].

B.2.1. Current Density on the Electrodes

The determination of electrode reaction kinetics hinges on understanding the current density, which is governed by the Butler-Volmer equation. This equation illustrates how the current density varies with the voltage difference between the electrodes (the overpotential) and the electrolyte concentration near the surface. The Butler-Volmer equation is given by:

$$j = j_0 \left\{ \exp\left[\frac{\alpha_a F \eta_s}{R_u T}\right] - \exp\left[-\frac{\alpha_c F \eta_s}{R_u T}\right] \right\}. \tag{B.5}$$

In Eq. B.5, j_0 represents the exchange current density, while α_a and α_c denote the charge transfer coefficients for the anode and cathode, respectively. The first term on the right side of the equation signifies the rate of the anodic reaction, whereas the second term represents the rate of the cathodic reaction. It is important to note that j_o depends on various factors such as reactant and product concentrations, temperature, and electrode-electrolyte characteristics.

Julius Tafel introduced a relationship between the current density and surface overpotential in 1905. For large values of η_s, one of the terms in Eq. B.5 dominates, leading to the following expression for the overall rate:

$$j = \begin{cases} j_0 \exp\left(\dfrac{\alpha_a F}{R_u T}\eta_s\right) & \text{for } \alpha_a F \eta_s \gg R_u T \\[2ex] -j_0 \exp\left(-\dfrac{\alpha_c F}{R_u T}\eta_s\right) & \text{for } \alpha_c F \eta_s \ll -R_u T \end{cases} \tag{B.6}$$

However, Eq. B.6 does not fully consider the concentration gradients near the electrode due to the electric double layer. To account for these effects, Dukovic and Tobias proposed Eq. B.7, which incorporates the local concentrations of different species throughout the electrode as,

$$j = j_0 \left[\left(\frac{c_{H_2}}{c_{H_2,0}}\right)^{\frac{1}{2}} \frac{c_{KOH}}{c_{KOH,0}} \exp\left(\frac{\alpha_a F \eta_s}{R_u T}\right) - \frac{c_{H_2O}}{c_{H_2O,0}} \exp\left(\frac{-\alpha_c F \eta_s}{R_u T}\right) \right] \tag{B.7}$$

where j_0 is the reference current density at the surface of the electrode, C_i is the concentration of species i at the surface of the electrode (but outside the EDL) and $C_{i,0}$ is the bulk concentration.